

# Towards constraining Dark Matter at the LHC: Higher order QCD predictions for $t\bar{t} + Z(Z \rightarrow \nu_\ell \bar{\nu}_\ell)$

G. Bevilacqua,<sup>a</sup> H. B. Hartanto,<sup>b</sup> M. Kraus,<sup>c</sup> T. Weber<sup>d</sup> and M. Worek<sup>d</sup>

<sup>a</sup>*MTA-DE Particle Physics Research Group, University of Debrecen, H-4010 Debrecen, PBox 105, Hungary*

<sup>b</sup>*Institute for Particle Physics Phenomenology, Department of Physics, Durham University, Durham, DH1 3LE, UK*

<sup>c</sup>*Humboldt-Universität zu Berlin, Institut für Physik, Newtonstraße 15, D-12489 Berlin, Germany*

<sup>d</sup>*Institute for Theoretical Particle Physics and Cosmology, RWTH Aachen University, D-52056 Aachen, Germany*

*E-mail:*

[giuseppe.bevilacqua@science.unideb.hu](mailto:giuseppe.bevilacqua@science.unideb.hu),

[heribertus.b.hartanto@durham.ac.uk](mailto:heribertus.b.hartanto@durham.ac.uk),

[manfred.kraus@physik.hu-berlin.de](mailto:manfred.kraus@physik.hu-berlin.de),

[tweber@physik.rwth-aachen.de](mailto:tweber@physik.rwth-aachen.de),

[worek@physik.rwth-aachen.de](mailto:worek@physik.rwth-aachen.de)

**ABSTRACT:** Triggered by ongoing dark matter searches in the top quark sector at the Large Hadron Collider we report on the calculation of the next-to-leading order QCD corrections to the Standard Model process  $pp \rightarrow t\bar{t} + Z(\rightarrow \nu_\ell \bar{\nu}_\ell)$ . This calculation is based on matrix elements for  $e^+ \nu_e \mu^- \bar{\nu}_\mu b\bar{b} \nu_\tau \bar{\nu}_\tau$  production and includes all non-resonant diagrams, interferences, and off-shell effects of the top quarks. Non-resonant and off-shell effects due to the finite  $W$ -boson width are also consistently taken into account. As it is common for such studies, we present results for both integrated and differential cross sections for a few renormalisation and factorisation scale choices and three different parton distribution functions. Already with the fairly inclusive cut selection and independently of the scale choice and the parton distribution function non-flat differential  $\mathcal{K}$ -factors are obtained for  $p_T^{miss}$ ,  $\Delta\phi_{\ell\ell}$ ,  $\Delta y_{\ell\ell}$ ,  $\cos\theta_{\ell\ell}$ ,  $H_T$ ,  $H'_T$  observables that are relevant for new physics searches. Good theoretical control over the Standard Model background is a fundamental prerequisite for a correct interpretation of possible signals of new physics that may arise in this channel. Thus, these observables need to be carefully reexamined in the presence of more exclusive cuts before any realistic strategies for the detection of new physics signal can be further developed. Since from the experimental point of view both  $t\bar{t}$  and  $t\bar{t} + Z(Z \rightarrow \nu_\ell \bar{\nu}_\ell)$  comprise the same final states, we additionally study the impact of the enlarged missing transverse momentum on various differential cross section distributions. To this end normalised differential distributions for  $pp \rightarrow e^+ \nu_e \mu^- \bar{\nu}_\mu b\bar{b} \nu_\tau \bar{\nu}_\tau$  and  $pp \rightarrow e^+ \nu_e \mu^- \bar{\nu}_\mu b\bar{b}$  are compared.

**KEYWORDS:** NLO Computations, QCD Phenomenology, Heavy Quark Physics

---

## Contents

<b>1</b>	<b>Introduction</b>	<b>1</b>
<b>2</b>	<b>Details of the calculation</b>	<b>6</b>
<b>3</b>	<b>Setup for numerical predictions</b>	<b>8</b>
<b>4</b>	<b>NLO QCD predictions for the LHC Run II energy of 13 TeV</b>	<b>11</b>
4.1	Integrated cross section and its scale dependence for the fixed scale	11
4.2	Integrated cross section and its scale dependence for the dynamical scale	12
4.3	Choosing the scale for differential cross sections	13
4.4	Impact of higher order corrections on new physics observables	19
4.5	Total missing transverse momentum distribution	21
4.6	PDF uncertainties	25
<b>5</b>	<b>Comparison to top anti-top pair production</b>	<b>27</b>
<b>6</b>	<b>Summary and Conclusions</b>	<b>30</b>

---

## 1 Introduction

Even though the Standard Model (SM) is currently the best description of all known elementary particles including interactions among them, it falls short of being a complete theory of fundamental interactions. On the one hand this self-consistent theory has demonstrated huge successes in explaining (almost) all experimental results and precisely predicted a wide variety of phenomena, on the other hand it leaves many important questions unanswered. Among others, the theory incorporates only three out of the four fundamental forces, omitting gravity and does not contain any viable dark matter (DM) particle that possesses all of the required properties deduced from observational cosmology. Thus, it is not surprising that searches for new physics beyond the SM are continuously carried out. Moreover, the hunt for the complete picture or at least answers to some of our questions, like for example, what dark matter is, is ongoing. Many experiments aimed at direct detection and the study of dark matter particles are actively undertaken, but none of them has been successful up until now. Therefore, if dark matter exists, unlike normal matter, it must barely interact with the known constituents of the SM. An alternative approach to the direct detection of dark matter particles in nature is to produce them in a laboratory. One of the candidates for a dark matter particle, as predicted by many theoretical models, is a weakly-interacting massive particle (WIMP). It is believed that this hypothetical particle is light enough to be produced at the Large Hadron Collider (LHC). At the LHC both ATLAS and CMS search for WIMP DM pair production in  $pp$  collisions. Since the DM particle does not interact with the SM particles it would not be detected directly. Simplified benchmark models for DM [1] assume, however, the existence of a mediator particle, which should couple both to

the SM particles and to the dark sector. A possible example for such a mediator is a spin zero particle that can be either a colour neutral scalar or pseudo-scalar particle. In the former case additionally mixing between the scalar mediator and the SM Higgs boson is assumed to be zero. Even though the nature of dark matter remains largely unknown, the couplings of the mediator to the SM fermions are strongly constrained by precision flavour measurements. Thus, the flavour structure of the new physics sector can not be generic, otherwise the non-standard contributions in flavour changing neutral current transitions would not be suppressed to a level consistent with experimental data. At this point the Minimal Flavour Violation (MFV) hypothesis [2] is often quoted, according to which the interaction between any new neutral spin zero state and SM fermions must be proportional to the fermion masses via Yukawa couplings. In other words, the SM Yukawa couplings are the only flavour symmetry breaking terms that are allowed in models beyond the SM if quark flavour mixing is to be protected. Because only the top quark has the Yukawa coupling of the order of one ( $Y_t = \sqrt{2}m_t/v \approx 1$ , where  $v$  is the Higgs vacuum expectation value) DM couples preferentially to top quarks in models with MFV. Thus, colour neutral mediators should be abundantly produced via loop induced gluon fusion or in association with  $t\bar{t}$  pairs. The signature for the former would exhibit missing transverse momentum ( $p_T^{miss}$ ) from non interacting DM particles that would be difficult to extract from the overwhelming QCD background. The signature for the latter would reveal event topologies consistent with the presence of top quarks, i.e. two oppositely charged leptons (electron and/or muons), jets identified as originating from bottom quarks and large missing transverse momentum, see the first Feynman diagram in Figure 1. Processes with similar final states might also occur in supersymmetric models including supersymmetric partners of the top quarks. In such models the direct decay of top squarks into the top quark and a neutralino might occur or top squarks can undergo a cascade decay through charginos and sleptons. In  $R$ -parity conserving models, the lightest neutralino is stable and all supersymmetric cascade-decays end up decaying into this particle which is undetected by ATLAS and CMS and whose existence can only be inferred by looking for unbalanced momentum. As a heavy, stable particle, the lightest neutralino is an excellent candidate to form the universe's cold dark matter. Representative Feynman diagrams are shown in Figure 1.

DM production in association with a top-quark pair ( $pp \rightarrow t\bar{t} + \chi\tilde{\chi} \rightarrow t\bar{t} + p_T^{miss}$ , where  $\chi$  stands for the WIMP) and top squark pair production ( $pp \rightarrow \tilde{t}\tilde{t} \rightarrow t\bar{t} + \tilde{\chi}_1^0\tilde{\chi}_1^0 \rightarrow t\bar{t} + p_T^{miss}$ , where  $\tilde{\chi}_1^0$  is considered to be the stable neutralino, i.e. the lightest supersymmetric particle (LSP)) have both been explored by the ATLAS and CMS collaborations within the 8 TeV [3, 4] and 13 TeV [5–10] data sets. The exclusion limits at 8 TeV have been based on an effective field theory approach, whereas the 13 TeV ones have been interpreted in the context of the simplified supersymmetric models with pair produced top squarks and in the context of simplified DM models with DM particle coupled to top quarks. Up until now no significant deviations with respect to the SM predictions have been observed. In all cases direct mass exclusion limits for new particles have been placed. In the case of DM scalar and pseudo-scalar mediator masses below 290 GeV and 300 GeV respectively have been excluded at 95% confidence level. These exclusion limits, as provided by the CMS experiment [10], are currently the most stringent limits derived at the LHC. One should mention at this point, however, that many assumptions enter such exclusion limits, among other a dark matter particle of 1 TeV and mediator couplings to fermions and dark

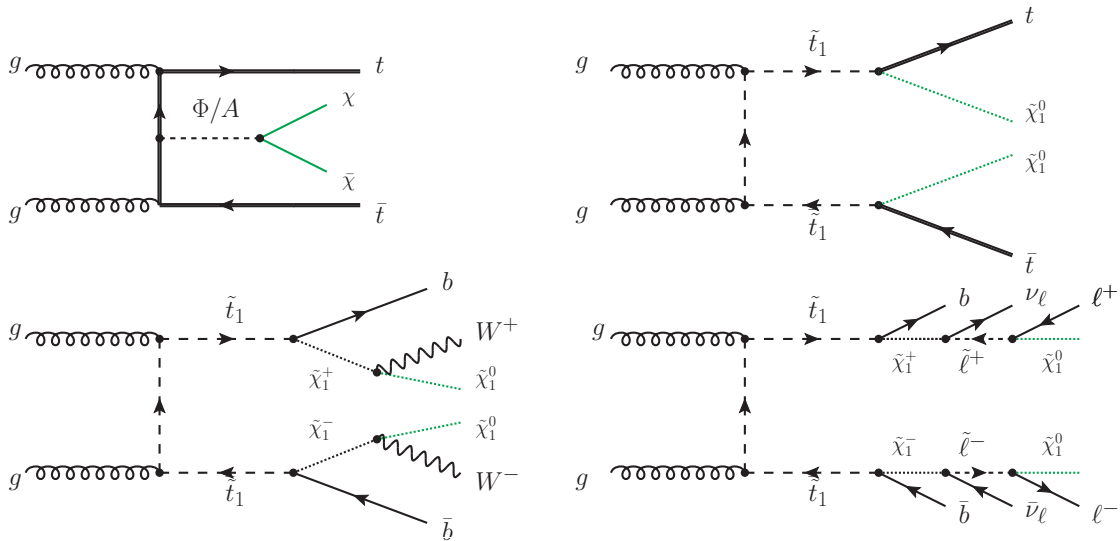


**Figure 1.** Representative Feynman diagrams for DM production (the first diagram) and for supersymmetric models with supersymmetric partners of the top quarks that might contribute to beyond the SM  $pp \rightarrow t\bar{t} + p_T^{miss}$  production at the LHC.

matter particles equal to unity have been usually assumed. Moreover, ATLAS and CMS's experimental results have been used to derive limits on a parameter space in particular in the effective field theory approach, see e.g. [11–14].

Independently of the underlying theoretical model the  $pp \rightarrow t\bar{t} + p_T^{miss}$  final state in the di-lepton top quark decay channel, where both  $W$  gauge bosons from  $t \rightarrow Wb$  decay further into  $W \rightarrow \ell\nu_\ell$ , is the most promising channel to look for new physics. The advantage of this channel in comparison to the semi-leptonic one lies in the fact that measurements of charged leptons (electrons and/or muons) are particularly precise at the LHC due to the excellent lepton energy resolution of the ATLAS and CMS detectors. Additionally, angular distributions of charged leptons are of huge importance since the  $CP$  nature of the coupling between the mediator and top quarks is encoded in the spin correlations of the top quark pair that can be probed via top quark decay products. Therefore, it is not surprising that the di-lepton channel is currently scrutinised by experimentalists using data recorded by the ATLAS and CMS collaborations in 2016. The new physics signal, however, needs to be extracted from the SM background processes. There are three distinct classes of major SM backgrounds that can resemble the features of the  $t\bar{t} + p_T^{miss}$  signal. The biggest (reducible) background (in absolute cross section value) comes from the  $t\bar{t}$  production process. Other processes that can be classified as the top quark background comprise  $t\bar{t}j$ ,  $tW$  and  $t\bar{t}W$ . Here neutrinos from  $W \rightarrow \ell\nu_\ell$  decays contribute to  $p_T^{miss}$ . Reducible non top quark backgrounds, on the other hand, comprise di-boson productions,  $W^+W^-$ ,  $W^\pm Z$  and  $ZZ$  as well as production of  $W$  and  $Z$  gauge boson in association with QCD light jets. For these background processes less jet activity is expected than for the signal process which can be further combined with the lack of bottom flavour jets. The common feature of both type of backgrounds, however, lies in the fact that background events populate low regions of the most relevant observables for the  $t\bar{t} + p_T^{miss}$  signature in the di-lepton channel, that consist of  $p_T^{miss}$  and  $M_{T2}$  [15]. Selecting events with a large amount of  $p_T^{miss}$ , asking for events with at least one  $b$ -jet and non-vanishing  $m_{\ell\ell}$  as well

as requiring that the missing transverse momentum and the transverse momentum of the two charged lepton system are well separated in the azimuthal angle,  $\Delta\phi(p_{T,\ell\ell}, p_T^{miss})$  [5], is sufficient to suppress overwhelming top backgrounds and other reducible background processes while keeping an adequate number of signal events.

The last and most important SM background comprises the irreducible  $t\bar{t} + Z$  background process. Here the  $p_T^{miss}$  signature arises from  $W \rightarrow \ell\nu_\ell$  and  $Z \rightarrow \nu_\ell\bar{\nu}_\ell$ . The  $t\bar{t} + Z$  production is the only process that provides extra genuine  $p_T^{miss}$ , thus, substantially adds to the tails of  $p_T^{miss}$  and  $M_{T2}$  distributions which are also populated by signal events. Indeed, various studies have shown that this residual background can survive all the selection cuts and the experimental sensitivity depends strongly on the proper modelling of  $t\bar{t}Z$  production, see e.g. [14]. Let us mention that in current analyses this background process is either simulated at leading order (LO) only or next-to-leading order (NLO) in QCD predictions for stable top quarks are combined with parton shower programs following the POWHEG or the MC@NLO matching procedure. Top quark decays are treated in the parton shower approximation omitting  $t\bar{t}$  spin correlations among other effects.

The goal of this paper is, therefore, to provide the state-of-the-art NLO QCD predictions for the SM  $t\bar{t}Z$  background process in the di-lepton top quark decay channel. More precisely, NLO QCD theoretical predictions to the  $e^+\nu_e\mu^-\bar{\nu}_\mu b\bar{b}\nu_\tau\bar{\nu}_\tau$  final state are calculated for the first time. All double-, single- and non-resonant Feynman diagrams, interferences, and off-shell effects of the top quarks are properly incorporated at the NLO level in QCD. Also non-resonant and off-shell effects due to the finite  $W$ -boson width are included. This calculation constitutes the first fully realistic NLO QCD computation for top quark pair production with additional missing  $p_T$  in hadronic collisions.

As a final comment, we note that NLO QCD corrections to the inclusive  $t\bar{t}Z$  production process (with on-shell top quarks and the  $Z$  gauge boson) have been calculated for the first time in Ref. [16] and afterwards recomputed in Refs. [17–20]. NLO QCD theoretical predictions from [18, 19] have additionally been matched with shower Monte Carlo (MC) programs using the POWHEL framework. The latter relies on POWHEG-BOX and allows for the matching between the fixed order computation at NLO in QCD (as provided by the HELAC-NLO MC program) and the parton shower evolution, followed by hadronization and hadron decays (as described by PYTHIA and HERWIG). In [18, 19] top quark and  $Z$  decays have been treated in the parton shower approximation omitting  $t\bar{t}$  spin correlations. Finally, in Ref. [21] improved calculations for  $pp \rightarrow t\bar{t}Z$  have been presented. This time NLO QCD corrections have been included to the production and (semi-leptonic) decays of top quarks in the narrow-width approximation (NWA), thus, also taking into account  $t\bar{t}$  spin correlations. Moreover, LO  $Z \rightarrow \ell^+\ell^-$  decays have been considered. Besides NLO QCD corrections, further step towards a more precise modeling of  $t\bar{t}Z$  have been achieved by including electroweak corrections [22] and soft gluon resummation effects [23, 24].

The paper is organised as follows. In Section 2, we briefly summarise the framework of our calculation and discuss technical aspects of the computation. Section 3 outlines the theoretical setup for LO and NLO QCD results. Results for the total cross sections and various differential cross sections are presented in Section 4. They are provided for the LHC centre-of-mass system energy of 13 TeV and for a few renormalisation and factorisation scale choices. The theoretical uncertainties, that are associated with neglected higher order terms in the perturbative expansion and with different parameterisations of the par-

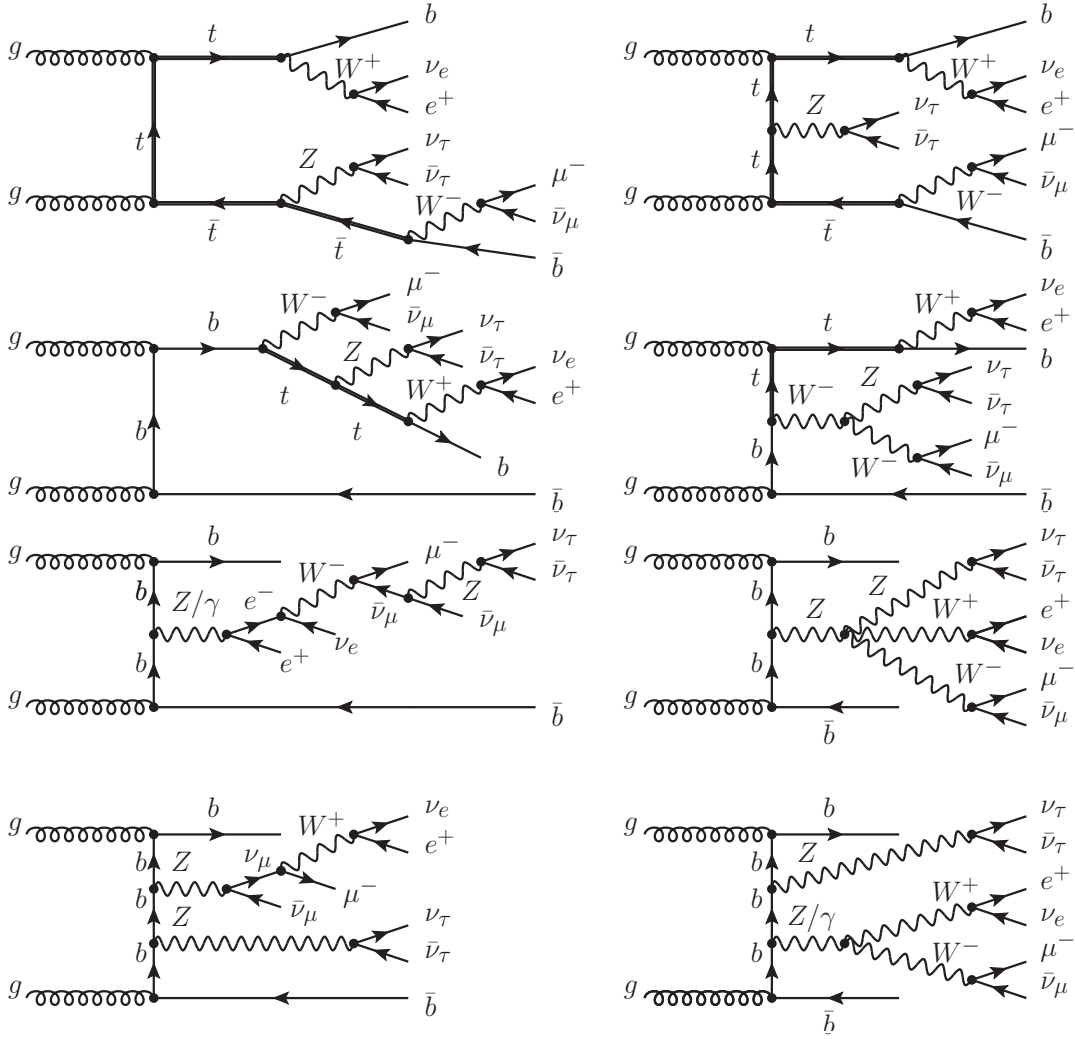


**Figure 2.** Representative Feynman diagrams with double- (first row), single- (second row) and no top quark resonances (third row) contributing to  $pp \rightarrow e^+ \nu_e \mu^- \bar{\nu}_\mu b \bar{b} \nu_\tau \bar{\nu}_\tau$  production at the leading order in perturbative expansion. Diagrams with a single  $W$  boson resonance that contribute to the off-shell effects of the  $W$  gauge boson are also presented (last row).

ton distribution functions, are also given. Additionally, we show differential cross section distributions, which are of particular interest for new physics searches. The latter comprise  $p_T^{miss}$ ,  $\Delta\phi_{\ell\ell}$ ,  $\Delta y_{\ell\ell}$ ,  $\cos\theta_{\ell\ell}$ ,  $H_T$  and  $H'_T$ . From the experimental point of view both  $t\bar{t}Z$  and  $t\bar{t}$  processes have the same signature, two charged leptons ( $\ell^\pm$ ), two bottom flavoured jets ( $j_b$ ) and missing transverse momentum from escaping neutrinos ( $p_T^{miss}$ ). Thus, in Section 5 we study the impact of the enlarged missing transverse momentum on various differential cross section distributions. To this end normalised differential distributions constructed from (anti-)top quark decay products for both  $pp \rightarrow e^+ \nu_e \mu^- \bar{\nu}_\mu b \bar{b} \nu_\tau \bar{\nu}_\tau$  and  $pp \rightarrow e^+ \nu_e \mu^- \bar{\nu}_\mu b \bar{b}$  are compared and discussed in that Section. Finally, in Section 6 our results are summarised and our conclusions are outlined.

## 2 Details of the calculation

At the LO level in perturbative expansion the  $e^+\nu_e\mu^-\bar{\nu}_\mu b\bar{b}\nu_\tau\bar{\nu}_\tau$  final states are produced via the scattering of either two gluons or one quark and the corresponding anti-quark. The  $\mathcal{O}(\alpha_s^2\alpha^6)$  contributions can be subdivided into three classes, diagrams containing two top quark propagators that can become resonant, diagrams containing only one top quark resonance and finally diagrams without any top quark resonance. Regarding the  $W^\pm$  resonances one can distinguish only two subclasses, double- and single-resonant gauge boson contributions. Examples of Feynman diagrams for each class are depicted in Figure 2. In total, there are 1024 LO diagrams for the  $gg \rightarrow e^+\nu_e\mu^-\bar{\nu}_\mu b\bar{b}\nu_\tau\bar{\nu}_\tau$  partonic reaction and 540 for each  $q\bar{q} \rightarrow e^+\nu_e\mu^-\bar{\nu}_\mu b\bar{b}\nu_\tau\bar{\nu}_\tau$  subprocess where  $q$  stands for up- or down-type quarks. Even-though we do not employ Feynman diagrams in our calculations we present their numbers as a measure of the complexity of the calculation. Instead, the calculation of scattering amplitudes is based on well-known off-shell iterative algorithms performed automatically within the HELAC-DIPOLES package [25], which avoids multiple evaluation of recurring building blocks. The results are cross checked with the HELAC-PHEGAS Monte Carlo (MC) program [26]. Phase space integration is performed and optimised with the help of PARNI [27] and KALEU [28]. Since the produced top quarks are unstable particles, the inclusion of the decays is performed in the complex mass scheme [29–32]. It fully respects gauge invariance and is straightforward to apply. Since we are interested in NLO QCD corrections, gauge bosons are treated within the fixed width scheme.

The virtual corrections comprise the 1-loop corrections to the LO reactions. These corrections can be classified into self-energy, vertex, box-type, pentagon-type, hexagon-type and heptagon-type corrections. In Table 1 the number of one-loop Feynman diagrams, that corresponds to each type of correction for the dominant  $gg \rightarrow e^+\nu_e\mu^-\bar{\nu}_\mu b\bar{b}\nu_\tau\bar{\nu}_\tau$  partonic subprocess as obtained with QGRAF [33], is given. We have cross-checked our results with the publicly available general purpose MC program MADGRAPH5-AMC@NLO [34]. Explicitly, we have compared results for the virtual NLO contribution to the squared amplitude,  $2\Re(\mathcal{M}_{tree}^*\mathcal{M}_{one-loop})$ , for a few phase-space points for  $gg$  and  $u\bar{u}$  partonic subprocesses and we have found perfect agreement in each case. In evaluating virtual corrections, the HELAC-1LOOP [35] MC library is used, that incorporates CUTTOOLS [36] and ONELOOP [37] as its cornerstones. The CUTTOOLS program contains an implementation of the OPP method for the reduction of one-loop amplitudes at the integrand level [38]. The ONELOOP library, on the other hand, is dedicated to the evaluation of the one-loop scalar functions. Renormalisation is done in the usual way by evaluating tree-level diagrams with counter-terms. For our process, we chose to renormalise the strong coupling in the  $\overline{\text{MS}}$  scheme with five active flavours and the top quark decoupled, while the mass renormalisation is performed in the on-shell scheme.

The real emission corrections to the LO process arise from tree-level amplitudes with one additional parton, i.e. an additional gluon, or a quark anti-quark pair replacing a gluon. For the calculation of the real emission contributions, the package HELAC-DIPOLES is employed. It implements the dipole formalism of Catani and Seymour [39, 40] for arbitrary helicity eigenstates and colour configurations of the external partons [25] and the Nagy-Soper subtraction scheme [41], which makes use of random polarisation and colour sampling of the external partons. Having two independent subtraction schemes in HELAC-DIPOLES allow us to cross check the correctness of the real corrections by comparing the two results.

ONE-LOOP CORRECTION	NUMBER OF FEYNMAN DIAGRAMS
SELF-ENERGY	17424
VERTEX	21544
BOX-TYPE	11726
PENTAGON-TYPE	4650
HEXAGON-TYPE	1038
HEPTAGON-TYPE	90
TOTAL NUMBER	56472

**Table 1.** The number of one-loop Feynman diagrams for the dominant  $gg \rightarrow e^+ \nu_e \mu^- \bar{\nu}_\mu b \bar{b} \nu_\tau \bar{\nu}_\tau$  partonic subprocess at  $\mathcal{O}(\alpha_s^3 \alpha^6)$  for the  $pp \rightarrow e^+ \nu_e \mu^- \bar{\nu}_\mu b \bar{b} \nu_\tau \bar{\nu}_\tau + X$  process. The Higgs boson exchange contributions are not considered and the Cabibbo-Kobayashi-Maskawa mixing matrix is kept diagonal.

PARTONIC SUBPROCESS	NUMBER OF FEYNMAN DIAGRAMS	NUMBER OF CS DIPOLES	NUMBER OF NS SUBTRACTIONS
$gg \rightarrow e^+ \nu_e \mu^- \bar{\nu}_\mu b \bar{b} \nu_\tau \bar{\nu}_\tau g$	6880	27	9
$gq \rightarrow e^+ \nu_e \mu^- \bar{\nu}_\mu b \bar{b} \nu_\tau \bar{\nu}_\tau q$	3520	15	5
$g\bar{q} \rightarrow e^+ \nu_e \mu^- \bar{\nu}_\mu b \bar{b} \nu_\tau \bar{\nu}_\tau \bar{q}$	3520	15	5
$q\bar{q} \rightarrow e^+ \nu_e \mu^- \bar{\nu}_\mu b \bar{b} \nu_\tau \bar{\nu}_\tau g$	3520	15	5

**Table 2.** The list of partonic subprocesses contributing to the subtracted real emission at  $\mathcal{O}(\alpha_s^3 \alpha^6)$  for the  $pp \rightarrow e^+ \nu_e \mu^- \bar{\nu}_\mu b \bar{b} \nu_\tau \bar{\nu}_\tau + X$  process where  $q = u, d, c, s$ . Also shown are the number of Feynman diagrams, as well as the number of Catani-Seymour and Nagy-Soper subtraction terms that correspond to these partonic subprocesses.

All partonic subprocesses that are taken into account for the real emission contributions are listed in Table 2, together with the number of the corresponding Feynman diagrams, the number of Catani-Seymour dipoles and Nagy-Soper subtraction terms. In each case, three times less terms are needed in the Nagy-Soper subtraction scheme compared to the Catani-Seymour scheme. The difference corresponds to the total number of possible spectators in the process under scrutiny, which are relevant in the Catani-Seymour case, but not in the Nagy-Soper case.

Let us note that HELAC-1LOOP and HELAC-DIPOLES are part of the HELAC-NLO framework [42] and that further technical details are described in Ref. [31, 43–45]. Let us also add that our theoretical predictions are stored in the form of (modified) Les Houches Event Files (LHEFs) [46] or ROOT [47] Ntuples. Building on [48], each event is stored with accessory matrix element and PDF information to allow re-weighting for different scale or

PDF choices. Storing events shows clear advantages when different observables are to be studied, or different kinematical cuts are to be applied, since no additional time-consuming running of the code is required.

### 3 Setup for numerical predictions

We consider the process  $pp \rightarrow e^+ \nu_e \mu^- \bar{\nu}_\mu b \bar{b} \nu_\tau \bar{\nu}_\tau$  for the LHC Run II centre-of-mass system energy of  $\sqrt{s} = 13$  TeV. We only simulate decays of the weak bosons to different lepton generations to avoid virtual photon singularities stemming from  $\gamma \rightarrow \ell^+ \ell^-$ . These interference effects are at the 0.2% level for inclusive cuts, as checked by an explicit leading order calculation performed with the help of the HELAC-PHEGAS MC framework. The  $\ell^\pm \ell^\mp$  cross section (with  $\ell_{1,2} = e, \mu$  since  $\tau$  leptons are always studied separately) can be obtained by multiplying the result with a lepton-flavor factor of 4. However, we additionally must count 3 different decays of the  $Z$  gauge boson ( $Z \rightarrow \nu_\ell \bar{\nu}_\ell$  with  $\nu_\ell = \nu_e, \nu_\mu, \nu_\tau$ ). Thus, the complete cross section can be realised by multiplying the results presented in the paper by 12. We keep the Cabibbo-Kobayashi-Maskawa mixing matrix diagonal. The following SM parameters are given within the  $G_\mu$  scheme that takes into account electroweak corrections related to the running of  $\alpha$

$$\begin{aligned} m_W &= 80.385 \text{ GeV}, & \Gamma_W &= 2.0988 \text{ GeV}, \\ m_Z &= 91.1876 \text{ GeV}, & \Gamma_Z &= 2.50782 \text{ GeV}, \\ G_\mu &= 1.166378 \times 10^{-5} \text{ GeV}^{-2}, & \sin^2 \theta_W &= 1 - m_W^2/m_Z^2. \end{aligned}$$

Leptonic  $W$  gauge boson decays do not receive NLO QCD corrections. To take some effects of higher order corrections into account for the gauge boson widths the NLO QCD values are used for LO and NLO matrix elements. The electroweak coupling is derived from the Fermi constant  $G_\mu$  according to

$$\alpha = \frac{\sqrt{2} G_\mu m_W^2 \sin^2 \theta_W}{\pi}. \quad (3.1)$$

The top quark mass is set to  $m_t = 173.2$  GeV. All other QCD partons including  $b$  quarks as well as leptons are treated as massless. Since we treat  $b$  quarks as massless partons there are no Higgs-exchange diagrams at tree level. Moreover, due to the negligibly small dependence on the Higgs boson mass, closed fermion loops which involve top quarks coupled to Higgs bosons, are neglected. The top quark width, as calculated from [49, 50], is taken to be  $\Gamma_t^{\text{LO}} = 1.47848$  GeV at LO and  $\Gamma_t^{\text{NLO}} = 1.35159$  GeV at NLO. The value of  $\alpha_s$  used for the top quark width  $\Gamma_t^{\text{NLO}}$  calculation is taken at  $m_t$ . This  $\alpha_s$  is independent of  $\alpha_s(\mu_0)$  that goes into the matrix element and PDF calculations. The latter is used to describe the dynamics of the whole process, the former only the top quark decays. Our calculation, like any fixed-order one, contains a residual dependence on the renormalisation scale ( $\mu_R$ ) and the factorisation scale ( $\mu_F$ ) arising from the truncation of the perturbative expansion in  $\alpha_s$ . As a consequence, observables depend on the values of  $\mu_R$  and  $\mu_F$  that are provided as input parameters. We assume that the default scale  $\mu_R = \mu_F = \mu_0$  is the same for both the renormalisation and factorisation scales. The scale systematics, however, is evaluated

by varying  $\mu_R$  and  $\mu_F$  independently in the range

$$\begin{aligned} \frac{1}{2} \mu_0 &\leq \mu_R, \mu_F \leq 2 \mu_0, \\ \frac{1}{2} &\leq \frac{\mu_R}{\mu_F} \leq 2, \end{aligned} \tag{3.2}$$

which in practice amounts to consider the following pairs

$$\left( \frac{\mu_R}{\mu_0}, \frac{\mu_F}{\mu_0} \right) = \left\{ (2, 1), (0.5, 1), (1, 2), (1, 1), (1, 0.5), (2, 2), (0.5, 0.5) \right\}. \tag{3.3}$$

We search for the minimum and maximum of the resulting cross sections. For  $\mu_0$  we consider two cases, the kinematic independent scale choice (fixed scale) and the kinematic dependent scale choice (dynamical scale). In the case of the integrated  $pp \rightarrow e^+ \nu_e \mu^- \bar{\nu}_\mu b \bar{b} \nu_\tau \bar{\nu}_\tau$  cross section both choices would be suitable to properly describe the production process. For the differential cross section distributions, however, the fixed scale would adequately describe the phase-space regions close to the  $t\bar{t}$  threshold but will fail at the tails of various dimensionful distributions. A proper dynamical scale choice, on the other hand, should characterise accurately all phase space regions. Specifically, we employ the following fixed scale

$$\mu_0 = m_t + \frac{m_Z}{2}, \tag{3.4}$$

commonly used in the studies of  $t\bar{t}Z$  production, see e.g. [16, 17, 19, 21], whereas for the dynamical scale a few choices will be examined. Firstly, we concentrate on the total transverse energy of the system,  $H_T$ , that is blind to the fact that in  $e^+ \nu_e \mu^- \bar{\nu}_\mu b \bar{b} \nu_\tau \bar{\nu}_\tau$  production Feynman diagrams with one or two top quark resonances might appear. Thus, the first dynamical scale choice is constructed according to

$$\mu_0 = \frac{H_T}{3}. \tag{3.5}$$

Here  $H_T$  is calculated on an event-by-event basis in line with

$$H_T = p_{T, e^+} + p_{T, \mu^-} + p_T^{miss} + p_{T, b_1} + p_{T, b_2}, \tag{3.6}$$

where  $b_1$  and  $b_2$  are bottom flavoured jets and the  $p_T^{miss}$  is the total missing transverse momentum from escaping neutrinos defined according to

$$p_T^{miss} = |\vec{p}_{T, \nu_e} + \vec{p}_{T, \bar{\nu}_\mu} + \vec{p}_{T, \nu_\tau} + \vec{p}_{T, \bar{\nu}_\tau}|. \tag{3.7}$$

In the next step the information about the underlying resonant nature of the process is used. To this end the following resonance aware dynamical scale choices, that we denote  $E_T$ ,  $E'_T$  and  $E''_T$ , are going to be inspected

$$\begin{aligned} \mu_0 &= \frac{E_T}{3} = \frac{1}{3} (m_{T, t} + m_{T, \bar{t}} + p_{T, Z}), \\ \mu_0 &= \frac{E'_T}{3} = \frac{1}{3} (m_{T, t} + m_{T, \bar{t}} + m_{T, Z}), \\ \mu_0 &= \frac{E''_T}{3} = \frac{1}{3} (m_{T, t} + m_{T, \bar{t}}). \end{aligned} \tag{3.8}$$

Here  $m_{T,i}$  is defined in accordance with  $m_{T,i} = \sqrt{p_{T,i}^2 + m_i^2}$ , where  $i$  stands for  $i = t, \bar{t}, Z$ . The top and anti-top quark as well as the  $Z$  gauge boson are reconstructed from their decay products assuming exact  $W$  and  $Z$  gauge bosons reconstruction and  $b$ -jet tagging efficiency of 100%, i.e.  $p(t) = p(j_{b_1}) + p(e^+) + p(\nu_e)$ ,  $p(\bar{t}) = p(j_{b_2}) + p(\mu^-) + p(\bar{\nu}_\mu)$  and  $p(Z) = p(\nu_\tau) + p(\bar{\nu}_\tau)$ , where  $j_{b_1}$  originates from the  $b$ -quark and  $j_{b_2}$  from anti- $b$  quark. To construct final state jets the IR-safe *anti- $k_T$*  jet algorithm [51] is employed with the resolution parameter  $R = 0.4$ . The *anti- $k_T$*  jet algorithm iterates recombinations of the final state partons with pseudo-rapidity  $|\eta| < 5$  until no partons are left and jets are created. We require at least two jets for our process, of which exactly two must be bottom flavoured jets. Moreover, we asked for two charged leptons and a large missing transverse momentum. We impose the following cuts on the transverse momenta and the rapidity of two recombined  $b$ -jets, which we assume to be always tagged

$$p_{T,b} > 40 \text{ GeV}, \quad |y_b| < 2.5, \quad \Delta R_{b\bar{b}} > 0.4. \quad (3.9)$$

The last cut, i.e. the separation between the  $b$ -jets, is implied by the jet algorithm. Basic selection cuts are applied to charged leptons to ensure that they are observed inside the detector and well separated from each other and from  $b$ -jets

$$p_{T,\ell} > 30 \text{ GeV}, \quad |y_\ell| < 2.5, \quad \Delta R_{\ell\ell} > 0.4, \quad \Delta R_{\ell b} > 0.4, \quad (3.10)$$

where  $\ell$  stands for the charged lepton:  $\mu^-, e^+$ . We additionally put a requirement on the missing transverse momentum  $p_T^{miss} > 50 \text{ GeV}$ . Finally, we place no restriction on the kinematics of the extra (light) jet.

The running of the strong coupling constant  $\alpha_s$  with two-loop (one-loop) accuracy at NLO (LO) is provided by the LHAPDF interface [52]. The number of active flavours is  $N_F = 5$ . Contributions induced by the bottom-quark parton density are neglected. At LO the  $b\bar{b}$  partonic subprocess contributes at the level of 1.1% to the  $q\bar{q}$  initial state. However, the full  $pp$  cross section is dominated by the  $gg$  channel (67%), thus, the  $b\bar{b}$  contribution to the  $pp \rightarrow e^+\nu_e\mu^-\bar{\nu}_\mu b\bar{b}\nu_\tau\bar{\nu}_\tau$  production process amounts to 0.4% only and can be safely disregarded. Following recommendations of PDF4LHC for the usage of parton distribution functions (PDFs) suitable for applications at the LHC Run II [53] we employ CT14 [54], which is the default PDF set in our studies, NNPDF3.0 [55] and MMHT14 [56].

We would like to stress that the above parameters and cuts on final states correspond to one particular setup. It is clear that there are many interesting phenomenological analyses that might be performed for the  $e^+\nu_e\mu^-\bar{\nu}_\mu b\bar{b}\nu_\tau\bar{\nu}_\tau$  process using our system with different setup. The latter could be chosen either in the context of the SM or having in mind searches for various new physics scenarios. Obviously, in each case a slightly different event selection would be required to optimise the search. Hence, in this publication we are not able to provide theoretical predictions for the irreducible background for each proposed BSM model. Instead, our main goal here is to demonstrate the size of higher order corrections to the  $e^+\nu_e\mu^-\bar{\nu}_\mu b\bar{b}\nu_\tau\bar{\nu}_\tau$  final state at the LHC in the presence of the inclusive cut selection that resembles as closely as possible the ATLAS and/or CMS detector responses. However, we shall also discuss the impact of NLO QCD corrections on a few observables that are relevant for new physics searches. If non-flat differential  $\mathcal{K}$ -factors are acquired for these observables already with a fairly inclusive cut selection and independently of the scale choice, these observables need to be carefully reexamined in the presence of more exclusive cuts before any realistic strategies for the detection of new physics signal can be further developed.

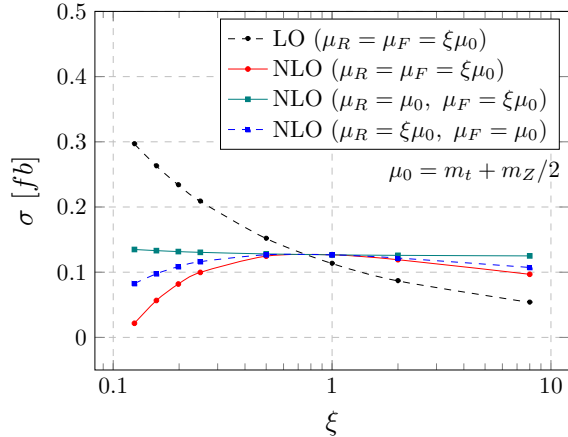


**Figure 3.** Scale dependence of the LO and NLO integrated cross section for the  $pp \rightarrow e^+ \nu_e \mu^- \bar{\nu}_\mu b \bar{b} \nu_\tau \bar{\nu}_\tau + X$  process at the LHC run II with  $\sqrt{s} = 13$  TeV. Renormalisation and factorisation scales are set to  $\mu_R = \mu_F = \xi \mu_0$  where  $\mu_0 = m_t + m_Z/2$  and  $\xi \in \{0.125, \dots, 8\}$ . The LO and NLO CT14 PDF sets are employed. Also shown is the variation of  $\mu_R$  with fixed  $\mu_F$  and the variation of  $\mu_F$  with fixed  $\mu_R$ .

## 4 NLO QCD predictions for the LHC Run II energy of 13 TeV

### 4.1 Integrated cross section and its scale dependence for the fixed scale

With the input parameters and cuts specified in Section 3, we arrive at the following predictions for  $\mu_R = \mu_F = \mu_0 = m_t + m_Z/2$

$$\begin{aligned} \sigma_{pp \rightarrow e^+ \nu_e \mu^- \bar{\nu}_\mu b \bar{b} \nu_\tau \bar{\nu}_\tau}^{\text{LO}}(\text{CT14}, \mu_0 = m_t + m_Z/2) &= 0.1133_{-0.0266}^{+0.0384} (33\%) \text{ fb}, \\ \sigma_{pp \rightarrow e^+ \nu_e \mu^- \bar{\nu}_\mu b \bar{b} \nu_\tau \bar{\nu}_\tau}^{\text{NLO}}(\text{CT14}, \mu_0 = m_t + m_Z/2) &= 0.1266_{-0.0075}^{+0.0014} (1.1\%) \text{ fb}. \end{aligned} \quad (4.1)$$

The full  $pp$  cross section receives positive and moderate NLO corrections of 12%. The theoretical uncertainties resulting from the scale variation and taken in a very conservative way as a maximum of the lower and upper bounds are 33% at LO and 5.9% at NLO. Thus, a reduction of the theoretical error by a factor of almost 6 is observed when higher order corrections are incorporated. In the case of truly asymmetric uncertainties, however, it is always more appropriate to symmetrise the errors. After symmetrisation the scale uncertainty at LO does not change substantially, i.e. it is reduced down to 29%. However, at the NLO in QCD the reduction is considerable as far as 3.5%. Therefore, by going from LO to NLO we have reduced the theoretical error by a factor of 8. Should we instead vary  $\mu_R$  and  $\mu_F$  simultaneously, up and down by a factor of 2 around  $\mu_0$ , the uncertainties would remain unchanged. This is due to the fact that the scale variation is driven solely by the changes in  $\mu_R$  as can be observed in Figure 3, where the graphical presentation of the behaviour of LO and NLO cross sections upon varying the scale by a factor  $\xi \in \{0.125, \dots, 8\}$  is shown for CT14 PDF sets.

Let us mention at this point that despite its relatively small cross section, a good theoretical control over the  $pp \rightarrow e^+ \nu_e \mu^- \bar{\nu}_\mu b \bar{b} \nu_\tau \bar{\nu}_\tau$  production process is phenomenologically relevant. This irreducible SM background at NLO in QCD is of the order of 1.5 fb, where a factor 12 has been used to obtain the complete cross section for the process. For comparison, typical predictions of new physics scenarios such as models with the vector,

SCALE CHOICE	$\sigma_{pp \rightarrow e^+ \nu_e \mu^- \bar{\nu}_\mu b \bar{b} \nu_\tau \bar{\nu}_\tau}$ [fb] <sup>LO</sup>	$\sigma_{pp \rightarrow e^+ \nu_e \mu^- \bar{\nu}_\mu b \bar{b} \nu_\tau \bar{\nu}_\tau}$ [fb] <sup>NLO</sup>	$\mathcal{K} = \sigma^{\text{NLO}}/\sigma^{\text{LO}}$
$\mu_0 = H_T/3$	$0.1260^{+0.0438 (35\%)}_{-0.0302 (24\%)}$	$0.1270^{+0.0009 (0.7\%)}_{-0.0086 (6.8\%)}$	1.01
$\mu_0 = E_T/3$	$0.1110^{+0.0368 (33\%)}_{-0.0258 (23\%)}$	$0.1272^{+0.0020 (1.6\%)}_{-0.0086 (6.8\%)}$	1.14
$\mu_0 = E'_T/3$	$0.1087^{+0.0359 (33\%)}_{-0.0251 (23\%)}$	$0.1268^{+0.0019 (1.5\%)}_{-0.0081 (6.4\%)}$	1.17
$\mu_0 = E''_T/3$	$0.1227^{+0.0423 (34\%)}_{-0.0293 (24\%)}$	$0.1286^{+0.0013 (1.0\%)}_{-0.0060 (4.7\%)}$	1.05

**Table 3.** LO and NLO cross sections for the  $pp \rightarrow e^+ \nu_e \mu^- \bar{\nu}_\mu b \bar{b} \nu_\tau \bar{\nu}_\tau + X$  process at the LHC run II with  $\sqrt{s} = 13$  TeV. Results for various scale choices are presented. Also included are theoretical errors as obtained from the scale variation. In the last column the  $\mathcal{K}$  factor, the ratio of the NLO to LO cross section, is given. The LO and NLO CT14 PDF sets are employed.

axial-vector, pseudoscalar, and scalar interaction between the top quark and the dark matter particle are also at the same level, see e.g. Refs. [13, 57–59]. Thus, our NLO analysis of  $pp \rightarrow e^+ \nu_e \mu^- \bar{\nu}_\mu b \bar{b} \nu_\tau \bar{\nu}_\tau$  at the LHC is a necessary step towards a correct interpretation of the possible signals of new physics that may arise in this channel.

## 4.2 Integrated cross section and its scale dependence for the dynamical scale

In the following we inspect our dynamical scale choices. Results for four cases,  $\mu_0 = H_T/3, E_T/3, E'_T/3$  and  $\mu_0 = E''_T/3$  are summarised in Table 3. They have been evaluated with the LO and NLO CT14 PDF sets. Also shown are theoretical errors as obtained from the scale variation and the corresponding  $\mathcal{K}$  factors. The latter are the ratios of the NLO to LO cross sections. All LO and NLO results agree very well with the corresponding predictions for the fixed scale within the quoted theoretical errors. Specifically, the agreement of  $0.05\sigma - 0.2\sigma$  ( $0.03\sigma - 0.4\sigma$ ) has been obtained at LO (NLO). Overall, no substantial reduction of theoretical uncertainties can be observed for integrated cross sections once a kinematic dependent scale is chosen. Specifically, for the LO cross section, after the symmetrisation of the theoretical error is applied, the theoretical error of the order of 28% – 29% can be reported. For the NLO case, on the other hand, the 2.8% – 4.1% range has been obtained. For all  $\mu_0$  the  $pp \rightarrow e^+ \nu_e \mu^- \bar{\nu}_\mu b \bar{b} \nu_\tau \bar{\nu}_\tau$  process receives positive and small (1% – 5%) to moderate (14% – 17%) NLO QCD corrections. Thus, judging just by the integrated cross section the case could be made that both  $\mu_0 = H_T/3$  and  $\mu_0 = E''_T/3$  combine two advantages, the smallest theoretical error and a small size of the higher order corrections as compared to the fixed scale choice. Of course, the importance of the dynamic scale does not lie in the calculation of the integrated cross section, which, after all, is a quite inclusive observable, hence less sensitive to the details of the scale choice. A place in which the dynamic scale must prove its usefulness is the correct description of various differential cross sections over a wide range of phase space, which are relevant from the point of view of top quark physics phenomenology. For completeness, in Figure 4 we present again the scale dependence of the LO and NLO integrated cross section for each case of  $\mu_0$ . The LO and the NLO CT14 PDF sets are employed. Also here a similar pattern as for  $\mu_0 = m_t + m_Z/2$  can be noticed, i.e. the independence of the NLO cross section from the variation of  $\mu_F$  while keeping fixed the value of  $\mu_R$ . Generally, from the point of view

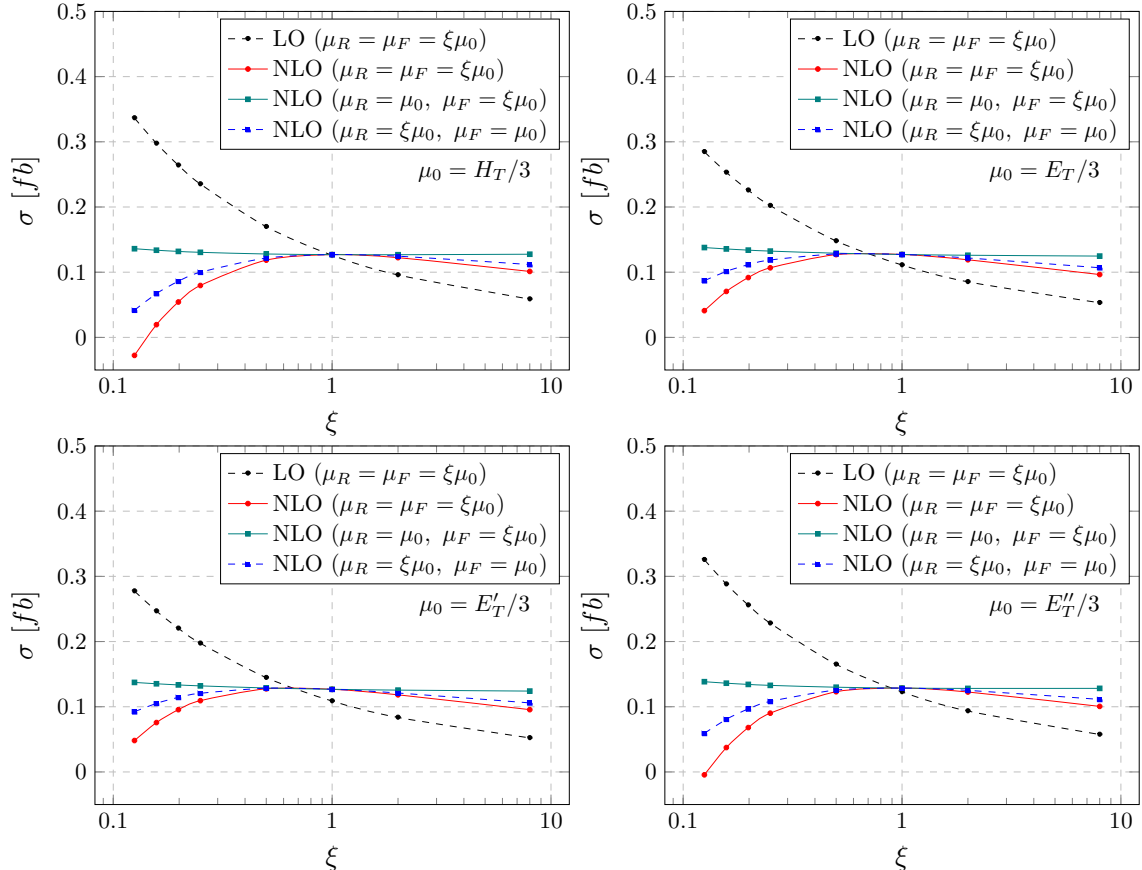


**Figure 4.** Scale dependence of the LO and NLO integrated cross section for the  $pp \rightarrow e^+ \nu_e \mu^- \bar{\nu}_\mu b \bar{b} \nu_\tau \bar{\nu}_\tau + X$  process at the LHC run II with  $\sqrt{s} = 13$  TeV. Renormalisation and factorisation scales are set to  $\mu_R = \mu_F = \xi \mu_0$  where  $\mu_0 = H_T/3, E_T/3, E'_T/3, E''_T/3$  and  $\xi \in \{0.125, \dots, 8\}$ . The LO and NLO CT14 PDF sets are employed. For each case of  $\mu_0$  also shown is the variation of  $\mu_R$  with fixed  $\mu_F$  and the variation of  $\mu_F$  with fixed  $\mu_R$ .

of the integrated  $\sigma_{pp \rightarrow e^+ \nu_e \mu^- \bar{\nu}_\mu b \bar{b} \nu_\tau \bar{\nu}_\tau}$  cross section each scale is a valid choice that might be used in real phenomenological applications.

### 4.3 Choosing the scale for differential cross sections

In the following we examine the size of NLO QCD corrections to various differential cross section distributions with the different scale choices that we have proposed in Section 3. The observables that we are going to present are obtained with our default CT14 PDF sets as well as for the cuts and parameters specified in the previous section. We start with the standard observables like for example the averaged transverse momentum and rapidity of the charged lepton ( $p_{T,\ell}, y_\ell$ ), and the averaged transverse momentum and rapidity of the  $b$ -jet ( $p_{T,b}, y_b$ ), the invariant mass of two  $b$ -jets ( $m_{bb}$ ), the invariant mass of two charged leptons ( $m_{\ell\ell}$ ) as well as the separation in the rapidity-azimuthal angle plane between the two  $b$ -jets and the two charged leptons ( $\Delta R_{bb}, \Delta R_{\ell\ell}$ ). By examining these observables we would like to establish which of the proposed dynamical scales is the most suitable for the description of the  $pp \rightarrow e^+ \nu_e \mu^- \bar{\nu}_\mu b \bar{b} \nu_\tau \bar{\nu}_\tau$  production process at the differential level in the presence of rather inclusive cuts on the final states. Ideally, we would be interested in the scale choice, which guarantees us small NLO QCD corrections in the whole plotted range for all observables and at the same time reduces theoretical uncertainties as compared to

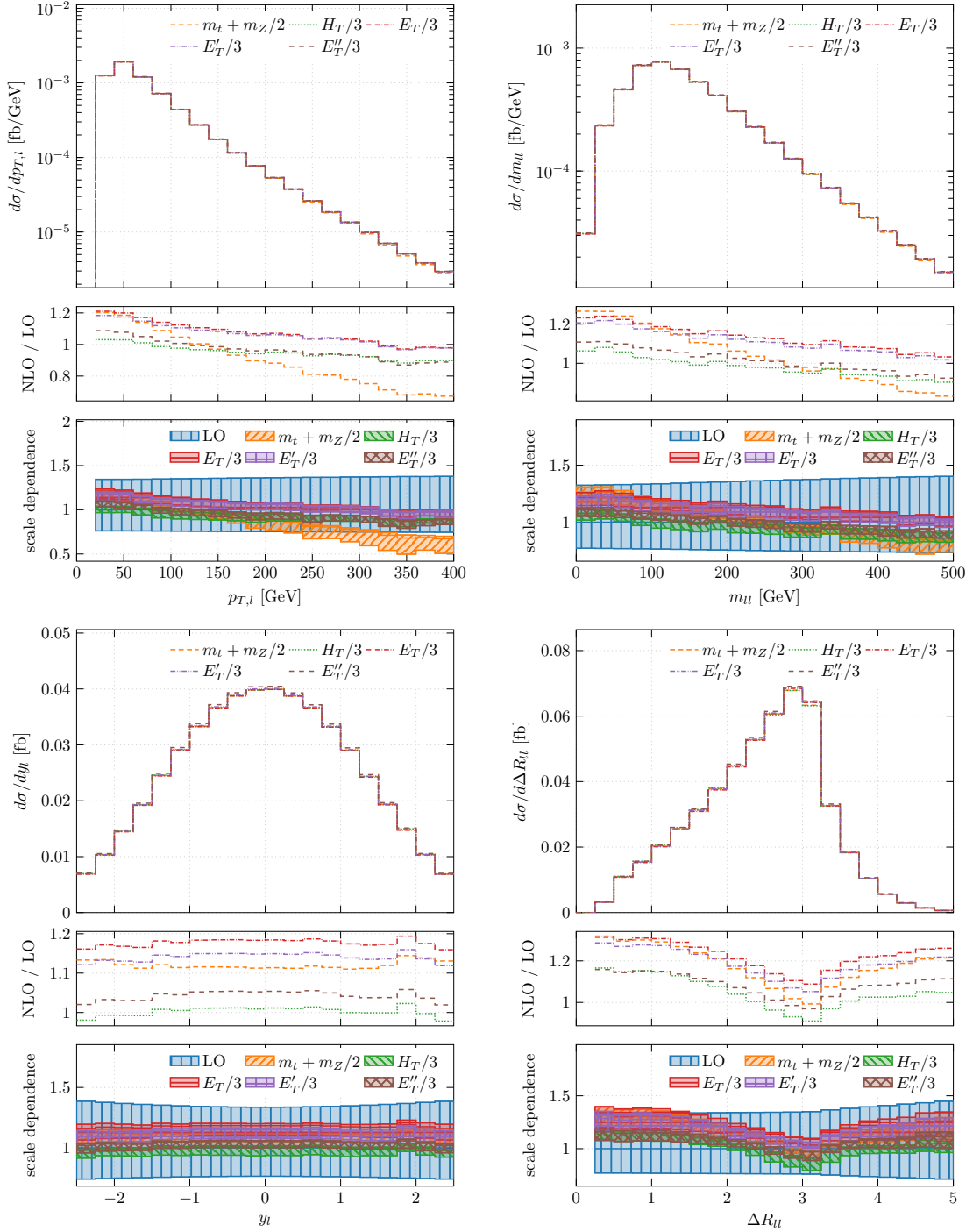


**Figure 5.** The  $pp \rightarrow e^+ \nu_e \mu^- \bar{\nu}_\mu b \bar{b} \nu_\tau \bar{\nu}_\tau + X$  differential cross section distribution as a function of (averaged)  $p_{T,\ell}$ ,  $m_{\ell\ell}$ , (averaged)  $y_\ell$  and  $\Delta R_{\ell\ell}$  at the LHC run II with  $\sqrt{s} = 13$  TeV. The upper plots show absolute NLO QCD predictions for various values of  $\mu_0$  where  $\mu_R = \mu_F = \mu_0$ . The middle panels display differential  $K$  factors. The lower panels present differential  $K$  factors together with the uncertainty band from the scale variation for various values of  $\mu_0$ . Also given is the relative scale uncertainties of the LO cross section for  $\mu_0 = m_t + m_Z/2$ . The LO and the NLO CT14 PDF sets are employed.

results obtained with the fixed scale choice. Thus, for comparison purposes we also present differential cross section results with  $\mu_R = \mu_F = \mu_0 = m_t + m_Z/2$ .

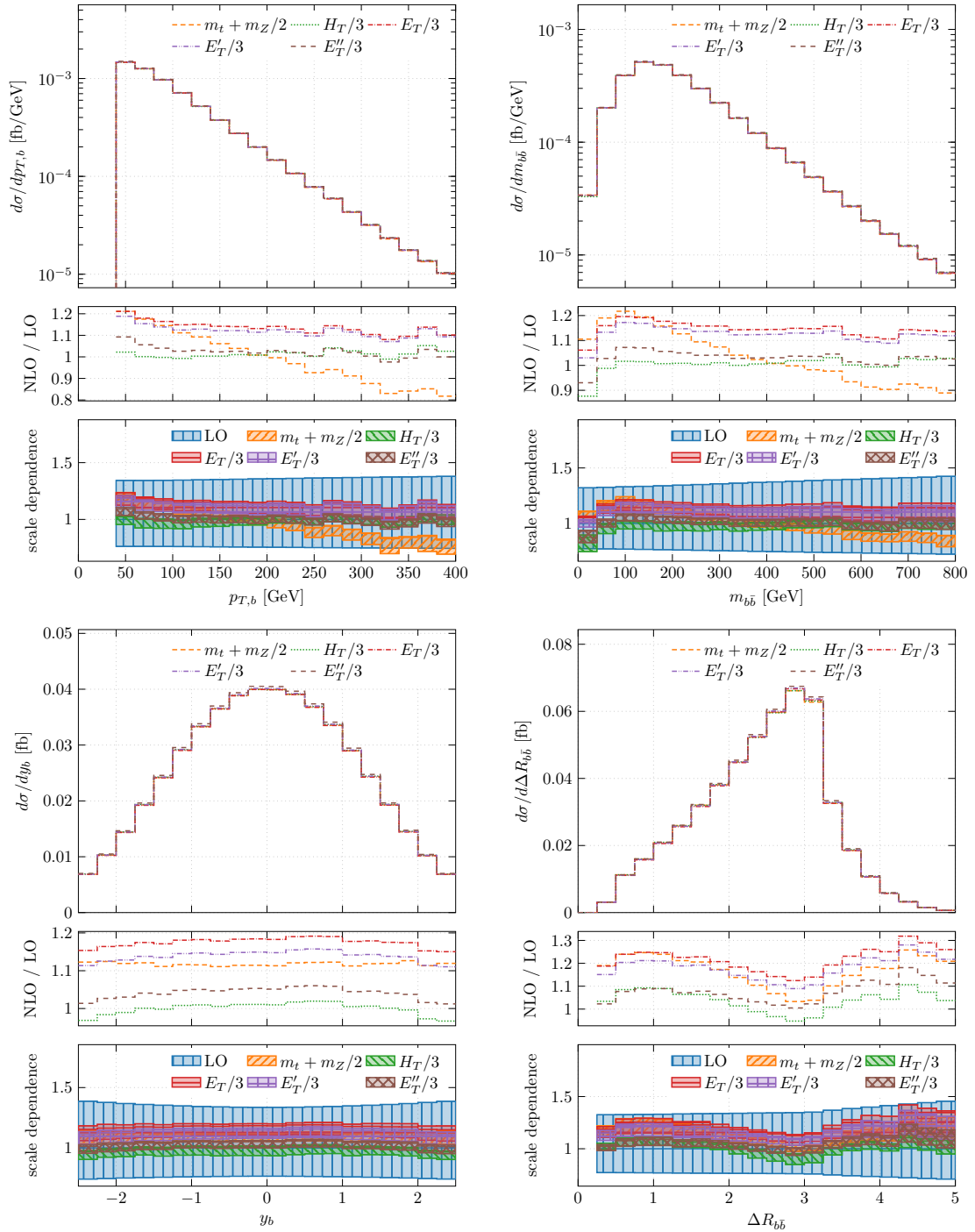


**Figure 6.** The  $pp \rightarrow e^+ \nu_e \mu^- \bar{\nu}_\mu b \bar{b} \nu_\tau \bar{\nu}_\tau + X$  differential cross section distribution as a function of (averaged)  $p_{T,b}$ ,  $m_{b\bar{b}}$ , (averaged)  $y_b$  and  $\Delta R_{b\bar{b}}$  at the LHC run II with  $\sqrt{s} = 13$  TeV. The upper plots show absolute NLO QCD predictions for various values of  $\mu_0$  where  $\mu_R = \mu_F = \mu_0$ . The middle panels display differential  $K$  factors. The lower panels present differential  $K$  factors together with the uncertainty band from the scale variation for various values of  $\mu_0$ . Also given is the relative scale uncertainties of the LO cross section for  $\mu_0 = m_t + m_Z/2$ . The LO and the NLO CT14 PDF sets are employed.

We start with the leptonic observables that are depicted in Figure 5. For each observable we present three plots. The upper plots show absolute NLO QCD predictions

for various values of  $\mu_0$  where  $\mu_R = \mu_F = \mu_0$ . The middle panels provide differential  $\mathcal{K}$  factors defined as  $\mathcal{K} = d\sigma^{\text{NLO}}(\mu_0)/d\sigma^{\text{LO}}(\mu_0)$ . The lower panels display the same differential  $\mathcal{K}$  factors together with the uncertainty bands from the scale variation. The latter are defined according to  $\mathcal{K}(\mu) = d\sigma^{\text{NLO}}(\mu)/d\sigma^{\text{LO}}(\mu)$ . Additionally, the LO blue bands are given to illustrate the relative scale uncertainty of the LO cross section. The latter are defined according to  $\mathcal{K}(\mu) = d\sigma^{\text{LO}}(\mu)/d\sigma^{\text{LO}}(\mu_0)$  for  $\mu_0 = m_t + m_Z/2$ . For the dimensionful observables  $p_{T,\ell}$  and  $m_{\ell\ell}$  we can observe perturbative instabilities in high energy tails of distributions in the case of  $\mu_0 = m_t + m_Z/2$  as can be seen from the lower panels. In these regions negative NLO QCD corrections of the order of 33% (17%) are visible for  $p_{T,\ell}$  ( $m_{\ell\ell}$ ). These results can be compared with the results for the dynamical scale choices where also negative but rather moderate higher order corrections of the order of 10%–11% (8%–10%) have been found for the tails of  $p_{T,\ell}$  ( $m_{\ell\ell}$ ) differential cross section distributions respectively with  $\mu_0 = H_T/3$  and  $\mu_0 = E_T''/3$ . Even though for  $\mu_0 = E_T/3$  and  $\mu_0 = E_T'/3$  we have obtained even smaller NLO QCD corrections in these regions, i.e. of the order of  $\pm(2\% - 3\%)$  only, the size of distortions is much larger for these scale choices. Consequently for  $\mu_0 = H_T/3$  and  $\mu_0 = E_T''/3$  flatter differential  $\mathcal{K}$ -factors are registered for these two observables. For a dimensionless observable  $y_\ell$  on the other hand almost constant corrections are obtained in the whole plotted range independently of the scale choice. What makes the result different for the various scale choices is the size of NLO QCD corrections. For the fixed scale as well as for  $\mu_0 = E_T/3$  and  $\mu_0 = E_T'/3$  they are positive and in the range of 12%–15% while for  $\mu_0 = H_T/3$  ( $\mu_0 = E_T''/3$ ) the maximum corrections received are of the order of  $\pm 2\%$ . Finally, for  $\Delta R_{\ell\ell}$  substantial distortions are noticed that are up to 32%, 26%, 23%, 24% and 19% respectively for  $\mu_0 = m_t + m_Z/2$ ,  $H_T/3$ ,  $E_T/3$ ,  $E_T'/3$  and  $E_T''/3$ .

In the next step we concentrate on theoretical uncertainties for these leptonic observables as estimated from scale variations at the NLO level in QCD. For the averaged transverse momentum of the charged lepton substantial scale variations are noticed at the end of the plotted spectrum, i.e. around 400 GeV for  $\mu_0 = m_t + m_Z/2$ . In these regions theoretical uncertainties taken conservatively as a maximum of the lower and upper bounds are  $\pm 25\%$  ( $\pm 14\%$  after symmetrisation). On the other hand for all presented dynamical scale choices they are reduced down to  $\pm 7\%$  ( $\pm 4\%$  after symmetrisation). In the latter case they are almost constant in the whole plotted range. These numbers can be compared to the LO scale uncertainties that for the fixed scale choice are up to  $\pm 41\%$  ( $\pm 34\%$ ). In the case of the invariant mass of the positron and the muon the difference between the fixed scale choice and the dynamical ones is milder. For  $\mu_0 = m_t + m_Z/2$  theoretical uncertainties up to  $\pm 11\%$  ( $\pm 6\%$ ) have been reached, whereas for  $\mu_0 = H_T/3$  up to  $\pm 9\%$  ( $\pm 4.5\%$ ). The latter is reduced down to  $\pm 7\%$  ( $\pm 3.5\%$ ) for other scales. This is a substantial reduction taking into account that at LO theoretical uncertainties up to  $\pm 41\%$  ( $\pm 34\%$ ) have been evaluated. As expected dimensionless observables have rather constant scale dependence independent of the scale choice. For  $\Delta R_{\ell\ell}$  we have obtained theoretical uncertainties around  $\pm 10\%$  ( $\pm 8\%$ ), whereas for  $y_\ell$  we have instead up to  $\pm 8\%$  ( $\pm 6\%$ ) for  $\mu_0 = m_t + m_Z/2$ ,  $E_T/3$  and  $\mu_0 = E_T'/3$  as well as up to  $\pm 6\%$  ( $\pm 3\%$ ) for  $\mu_0 = H_T/3$  and  $\mu_0 = E_T''/3$ . These outcomes can be compared to  $\pm 43\%$  ( $\pm 36\%$ ) and  $\pm 37\%$  ( $\pm 31\%$ ) uncertainties at the LO level respectively for  $\Delta R_{\ell\ell}$  and  $y_\ell$  with  $\mu_0 = m_t + m_Z/2$ .

Similar conclusions can be drawn for the  $b$ -jet kinematics that is shown in Figure 6. For the averaged  $p_T$  distribution of the bottom jet at the end of the plotted range negative

NLO QCD corrections of the order of 18% are acquired for  $\mu_0 = m_t + m_Z/2$ . This can be compared with positive 20% corrections at the beginning of the spectrum which resulted in distortions of the order of 40%. The situation is substantially improved for the case of  $\mu_0 = H_T/3$  where positive higher order QCD corrections below 5% are attained for  $p_{T,b} \in [40, 400]$  GeV. For the remaining three scale choices the similar size of distortions of the order of 10% have been observed. For the invariant mass of the two  $b$ -jet system the best scale choice seems to be again  $\mu_0 = H_T/3$  for which rather constant corrections, with the exception of the beginning of the spectrum, are visible. The former are of the order of +3%, the latter are up to -12%. This can be contrasted with results for  $\mu_0 = m_t + m_Z/2$  where we have obtained NLO corrections ranging from +22% down to -11%. Looking at the dimensionless observable like for example the averaged rapidity of the  $b$ -jet we have noticed almost constant NLO QCD corrections in the considered range  $y_b \in [-2.5, 2.5]$ . The smallest corrections of the order of -3% and +2% have been obtained respectively for  $\mu_0 = H_T/3$  and  $\mu_0 = E''/3$ . On the other hand the largest corrections, up to even +18%, have been received for  $\mu_0 = E_T/3$ . For the fixed scale choice they are only up to +13%. Finally, for the last standard observable that we have studied, which is  $\Delta R_{b\bar{b}}$ , we can recommend  $\mu_0 = H_T/3$  for which NLO QCD corrections maximally up to +10% and distortions up to 15% have been gained. By comparison the distortions are the most severe for the fixed scale choice. They amount even up to 22%.

In the following we move to the NLO theoretical uncertainties for observables that describe the kinematics of the bottom jets. Once more we notice that for the fixed scale choice represented by  $\mu_0 = m_t + m_Z/2$  and for dimensionful observables like for example the averaged transverse momentum of the  $b$ -jet,  $p_{T,b}$ , theoretical uncertainties are outside the LO bands at the end of the plotted range. Nevertheless taken conservatively they are rather moderate of the order of  $\pm 15\%$  ( $\pm 8\%$  after symmetrisation) in that region. The size and perturbative behaviour is modified when the dynamical scale choice is applied. For  $\mu_0 = H_T/3$  and  $\mu_0 = E''/3$  theoretical errors are reduced by more than a factor of 2, down to  $\pm 7\%$  ( $\pm 4\%$ ) and  $\pm 6\%$  ( $\pm 4\%$ ) respectively. We also note that employing the dynamical scale choices caused NLO bands to lie within the LO ones as one would expect from a well-behaved perturbative expansion in  $\alpha_s$ . For the invariant mass of the two  $b$ -jet system we have a similar behaviour. For results with  $\mu_0 = m_t + m_Z/2$  the theoretical uncertainties up to  $\pm 11\%$  ( $\pm 6\%$ ) have been obtained, whereas in the case of  $\mu_0 = H_T/3$ ,  $E_T''/3$  decreased theoretical uncertainties up to only  $\pm 8\%$  ( $\pm 5\%$ ) have been estimated. In both cases the improvement with respect to the LO theoretical uncertainties is dramatic since we have  $\pm 41\%$  ( $\pm 34\%$ ) for  $p_{T,b}$  and  $\pm 44\%$  ( $\pm 36\%$ ) for  $m_{b\bar{b}}$ . Considering angular distributions like  $y_b$  and  $\Delta R_{b\bar{b}}$  we have rather constants theoretical uncertainties below 8% independent of the scale choice for the former and below 10% for the later. After symmetrisation is applied they go below 5% and 8% respectively. Whereas at the LO level they are up to  $\pm 37\%$  ( $\pm 31\%$ ) and  $\pm 44\%$  ( $\pm 36\%$ ).

Combining information about the size of NLO QCD corrections and NLO QCD theoretical uncertainties we conclude that either scale  $\mu_0 = H_T/3$  or  $\mu_0 = E''/3$  should be employed at the differential level for the adequate description of the standard observables in the  $e^+ \nu_e \mu^- \bar{\nu}_\mu b \bar{b} \nu_\tau \bar{\nu}_\tau$  production process at the LHC with a centre of mass system energy of  $\sqrt{s} = 13$  TeV in the presence of rather inclusive cuts on the measured final states.

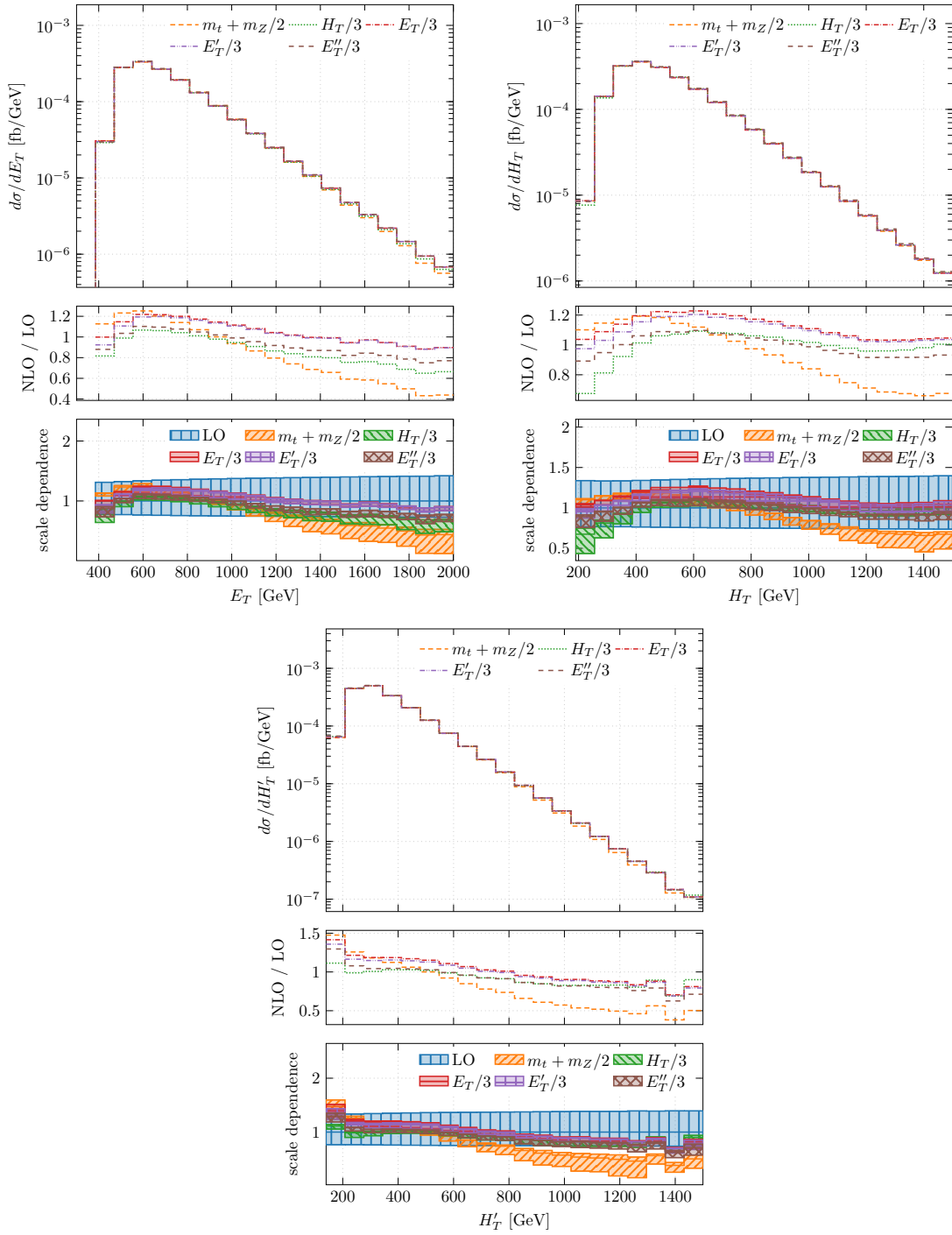


**Figure 7.** The  $pp \rightarrow e^+ \nu_e \mu^- \bar{\nu}_\mu b \bar{b} \nu_\tau \bar{\nu}_\tau + X$  differential cross section distribution as a function of  $E_T$ ,  $H_T$  and  $H'_T$  at the LHC run II with  $\sqrt{s} = 13$  TeV. The upper plots show absolute NLO QCD predictions for various values of  $\mu_0$  where  $\mu_R = \mu_F = \mu_0$ . The middle panels display differential  $\mathcal{K}$  factors. The lower panels present differential  $\mathcal{K}$  factors together with the uncertainty band from the scale variation for various values of  $\mu_0$ . Also given is the relative scale uncertainties of the LO cross section for  $\mu_0 = m_t + m_Z/2$ . The LO and the NLO CT14 PDF sets are employed.

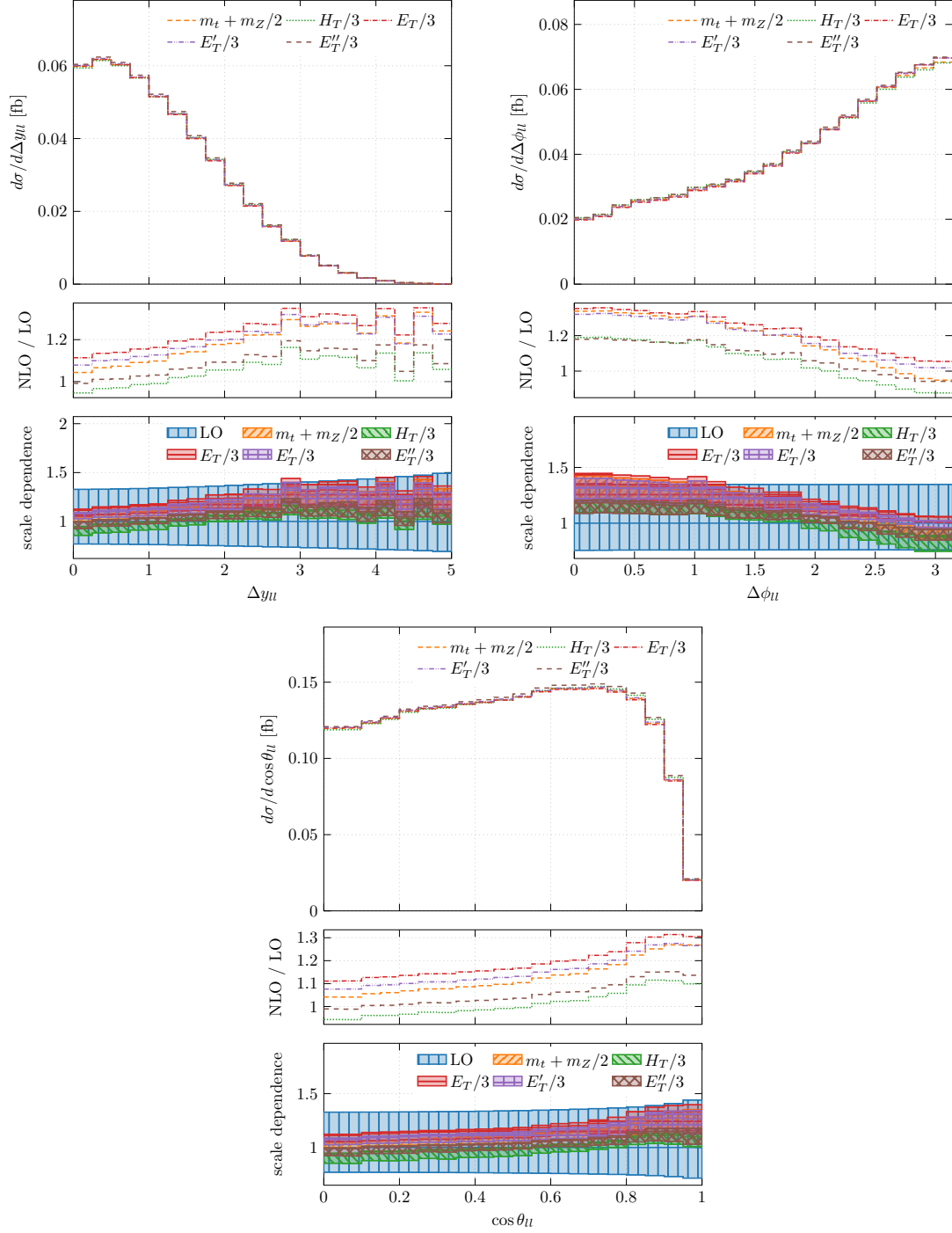


**Figure 8.** The  $pp \rightarrow e^+ \nu_e \mu^- \bar{\nu}_\mu b \bar{b} \nu_\tau \bar{\nu}_\tau + X$  differential cross section distribution as a function of  $\Delta y_{\ell\ell} = |y_{\ell_1} - y_{\ell_2}|$ ,  $\Delta\phi_{\ell\ell} = |\phi_{\ell_1} - \phi_{\ell_2}|$  and  $\cos\theta_{\ell\ell} = \tanh(\Delta y_{\ell\ell}/2)$  at the LHC run II with  $\sqrt{s} = 13$  TeV. The upper plots show absolute NLO QCD predictions for various values of  $\mu_0$  where  $\mu_R = \mu_F = \mu_0$ . The middle panels display differential K factors. The lower panels present differential K factors together with the uncertainty band from the scale variation for various values of  $\mu_0$ . Also given is the relative scale uncertainties of the LO cross section for  $\mu_0 = m_t + m_Z/2$ . The LO and the NLO CT14 PDF sets are employed.

#### 4.4 Impact of higher order corrections on new physics observables

Moving forward we employ our recommended scale choices  $\mu_0 = H_T/3$  and  $\mu_0 = E''/3$  to discuss the size of NLO QCD corrections to a few observables that are relevant in the

context of dark matter searches. Among others we have identified six observables, three dimensionful and three dimensionless. Specifically, we have studied the total transverse energy,  $E_T$ , as given by

$$E_T = \sqrt{p_T^2(t) + m_t^2} + \sqrt{p_T^2(\bar{t}) + m_t^2} + \sqrt{p_T^2(Z) + m_Z^2}, \quad (4.2)$$

and the total transverse momentum of the  $t\bar{t}Z$  system,  $H_T$ . The total transverse momentum build only from the visible final states and denoted as  $H'_T$  is also investigated. The latter two are defined according to

$$\begin{aligned} H_T &= p_{T,b_1} + p_{T,b_2} + p_{T,e^+} + p_{T,\mu^-} + p_T^{miss}, \\ H'_T &= p_{T,b_1} + p_{T,b_2} + p_{T,e^+} + p_{T,\mu^-}. \end{aligned} \quad (4.3)$$

We investigate additionally the rapidity separation of the two charged leptons,  $\Delta y_{\ell\ell} = |y_{\ell_1} - y_{\ell_2}|$ , the azimuthal angle difference between the two leptons,  $\Delta\phi_{\ell\ell} = |\phi_{\ell_1} - \phi_{\ell_2}|$  and  $\cos\theta_{\ell\ell}$  constructed according to the following formula

$$\cos\theta_{\ell\ell} = \tanh(\Delta y_{\ell\ell}/2). \quad (4.4)$$

The angular distributions of the charged leptons resulting from top decays carry information about the spin correlations between the final-state top quarks. Thus, they can be used for example to study the CP nature of the coupling between the mediator particle and top quarks in various dark matter scenarios, see e.g. [14]. Proper modelling for these observables within the SM is a fundamental requirement for a correct interpretation of the possible signals of new physics that may arise in the  $pp \rightarrow t\bar{t} + p_T^{miss}$  channel.

In Figure 7 we present the differential cross section distribution as the function of  $E_T$ ,  $H_T$  and  $H'_T$ . For comparison reasons also for these observables predictions for all scale choices for  $\mu_0 = \mu_F = \mu_R$  are depicted. In the case of  $E_T$ , negative and substantial NLO QCD corrections up to 34%, 23% and 56% are obtained around 2 TeV respectively for  $\mu_0 = H_T/3$ ,  $\mu_0 = E_T''/3$  and  $\mu_0 = m_t + m_Z/2$ . Overall shape distortions are of the order of 15%, 11% for the dynamical scale choices and around 69% for the fixed scale choice. NLO theoretical uncertainties from the scale dependence are up to  $\pm 27\%$  ( $\pm 16\%$  after symmetrisation),  $\pm 17\%$  ( $\pm 10\%$ ) and  $\pm 72\%$  ( $\pm 46\%$ ) respectively for  $\mu_0 = H_T/3$ ,  $\mu_0 = E_T''/3$  and  $\mu_0 = m_t + m_Z/2$ . A similar pattern could be seen for  $H_T$  and  $H'_T$ . In the former case for  $\mu_0 = E_T''/3$  NLO QCD corrections are negative and moderate up to 7% at around 1.5 TeV. When comparing the threshold region above 190 GeV with the end of the plotted range, shape distortions of the order of 4% are only detected for this scale. On the other hand, for other two choices  $\mu_0 = H_T/3$  and  $\mu_0 = m_t + m_Z/2$  large and negative NLO QCD corrections at the level of 32% have been perceived, respectively either at the beginning or at the end of the  $H_T$  spectrum. Consequently, shape distortions are of the order of 33% and 43% for the dynamical and fixed values of  $\mu_0$ . For the scale dependence we can reach  $\pm 15\%$  ( $\pm 9\%$ ) close to the threshold and  $\pm 8\%$  ( $\pm 5\%$ ) around 1.5 TeV for  $\mu_0 = E_T''/3$ . Whereas predictions with  $\mu_0 = H_T/3$  and  $\mu_0 = m_t + m_Z/2$  have substantially larger theoretical errors up to  $\pm 35\%$  ( $\pm 23\%$ ) for  $\mu_0 = H_T/3$  (at the beginning of the spectrum of  $H_T$ ) and up to  $\pm 27\%$  ( $\pm 16\%$ ) for  $\mu_0 = m_t + m_Z/2$  (at the end of the plotted spectrum of  $H_T$ ). Finally, we examine the simplified version of  $H_T$ , namely  $H'_T$ . As already advertised the latter comprises only visible final states, i.e. charged leptons as well as the two bottom jets

and it is frequently used by experimental groups to look for new physics in top quark pair production. The observable received rather large higher order corrections at the end of the plotted spectrum as compared to  $H_T$ . Specifically, we have negative NLO QCD corrections of the order of 50% for the fixed scale choice and up to 29% for  $\mu_0 = E_T''/3$ . On the other hand, for  $\mu_0 = H_T/3$  negative but moderate corrections up to only 10% are observed. NLO shape distortions are of the order of 97%, 58% and 21% respectively for  $\mu_0 = m_t + m_Z/2$ ,  $\mu_0 = E_T''/3$ , and  $\mu_0 = H_T/3$ . Clearly, the differential  $\mathcal{K}$ -factors are far from flat, showing major changes in the shape of the observables when the QCD corrections of the order of  $\alpha_s$  are incorporated. When investigating scale uncertainties for the  $H_T'$  observable we noticed their similarities to the case of  $H_T$ . In detail, we have estimated theoretical errors up to  $\pm 34\%$  ( $\pm 24\%$ ),  $\pm 19\%$  ( $\pm 14\%$ ), and  $\pm 10\%$  ( $\pm 7\%$ ) individually for  $\mu_0 = m_t + m_Z/2$ ,  $\mu_0 = E_T''/3$ , and  $\mu_0 = H_T/3$ .

Leptonic angular distributions, i.e.  $\Delta y_{\ell\ell}$ ,  $\Delta\phi_{\ell\ell}$  and  $\cos\theta_{\ell\ell}$ , are depicted in Figure 8. For the rapidity difference of the two charged leptons we observe small corrections of the order of a few percent for  $\mu_0 = H_T/3$  and  $\mu_0 = E_T''/3$ . By comparison for  $\mu_0 = m_t + m_Z/2$  they can reach even 16%. Overall shape distortions at NLO for these scale choices are 2.5%, 5% and 12%, respectively. For the opening angle between the two charged leptons, on the other hand, already for both dynamical scale choices positive corrections up to 19% are visible, whereas for the fixed scale choice they are up to 34% in the same region. Also shape distortions are substantially larger for this observable, i.e. they are at the level of 31%, 23% and 39%. Finally,  $\cos\theta_{\ell\ell}$  has received rather moderate NLO QCD corrections up to 10% for  $\mu_0 = H_T/3$  and up to 14% for  $\mu_0 = E_T''/3$ . Also in this case higher order corrections for the fixed scale choice are substantially larger, reaching 27%. Shape distortions are at the level of 17% ( $\mu_0 = H_T/3$ ), 15% ( $\mu_0 = E_T''/3$ ) and 23% ( $\mu_0 = m_t + m_Z/2$ ). When examining the scale dependence for these observables we can see a similar size of theoretical errors regardless of what scale we choose. The theoretical uncertainties are also similar in size for all three angular observables. Specifically, for  $\Delta y_{\ell\ell}$  they are up to  $\pm 9\%$  ( $\pm 6\%$  after symmetrisation) for the dynamical scale choice and up to  $\pm 12\%$  ( $\pm 10\%$ ) for the fixed scale choice. In the case of  $\Delta\phi_{\ell\ell}$  they are below  $\pm 10\%$  ( $\pm 5\%$ ) for  $\mu_0 = E_T''/3$  and ( $\mu_0 = m_t + m_Z/2$ ), while for ( $\mu_0 = H_T/3$ ) they are slightly higher up to  $\pm 15\%$  ( $\pm 8\%$ ). Lastly, for  $\cos\theta_{\ell\ell}$  scale dependence is of the order of  $\pm 10\%$  ( $\pm 5\%$ ). Well behaved as they are, these leptonic observables can be now safely exploited to probe new physics at the LHC.

#### 4.5 Total missing transverse momentum distribution

Among all infrared safe observables in  $e^+\nu_e\mu^-\bar{\nu}_\mu b\bar{b}\nu_\tau\bar{\nu}_\tau$  production the total missing transverse momentum, denoted as  $p_T^{miss}$ , plays a special role. Thus, we discuss it separately in this section. The observation of an excess in  $p_T^{miss}$  represents an important signature in various BSM and DM models. The signals from new physics need to be extracted from the SM background, hence an accurate modelling of the  $p_T^{miss}$  observable in the  $t\bar{t} + p_T^{miss}$  channel, particularly in the high- $p_T$  region, is crucial. Given that neutral weakly interacting particles (such as neutrinos, dark matter candidates or the lightest SUSY neutralino) escape from the LHC detectors, the presence of such particles can only be inferred through the observation of a momentum imbalance in the final state. In the process under consideration there are four particles contributing to the total missing transverse momentum: two neutrinos ( $\nu_e, \bar{\nu}_\mu$ ) ascribed to the top quark decays and two neutrinos ( $\nu_\tau, \bar{\nu}_\tau$ ) originated from the decay of the  $Z$  gauge boson. Although these particles have different origin and

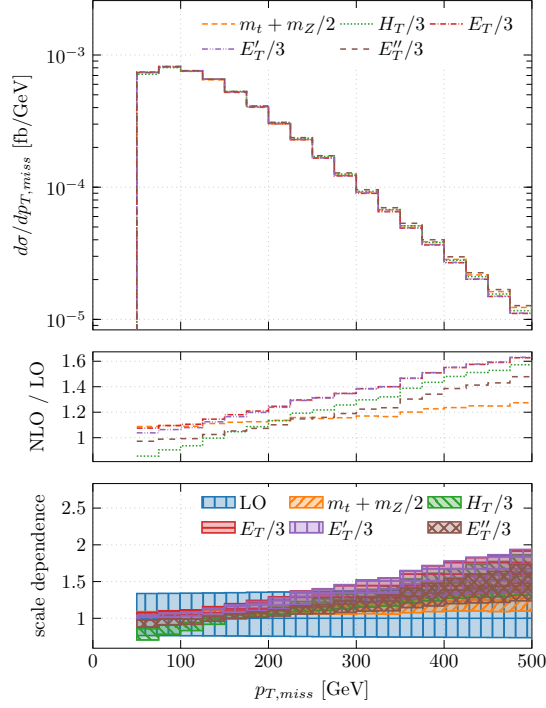


**Figure 9.** The  $pp \rightarrow e^+ \nu_e \mu^- \bar{\nu}_\mu b \bar{b} \nu_\tau \bar{\nu}_\tau + X$  differential cross section distribution as a function of  $p_T^{miss}$  at the LHC run II with  $\sqrt{s} = 13$  TeV. The upper plots show absolute NLO QCD predictions for various values of  $\mu_0$  where  $\mu_R = \mu_F = \mu_0$ . The middle panels display differential  $\mathcal{K}$  factors. The lower panels present differential  $\mathcal{K}$  factors together with the uncertainty band from the scale variation for various values of  $\mu_0$ . Also given is the relative scale uncertainties of the LO cross section for  $\mu_0 = m_t + m_Z/2$ . The LO and the NLO CT14 PDF sets are employed.

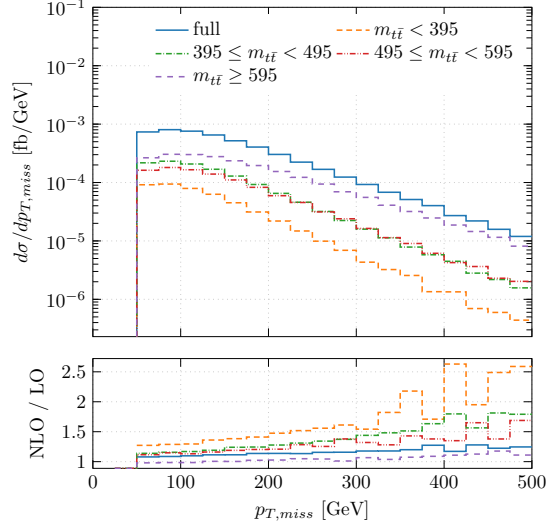


**Figure 10.** The  $pp \rightarrow e^+ \nu_e \mu^- \bar{\nu}_\mu b \bar{b} \nu_\tau \bar{\nu}_\tau + X$  double differential cross section distribution as a function of  $p_T^{miss}$  and  $m_{t\bar{t}}$  at the LHC run II with  $\sqrt{s} = 13$  TeV. The upper plot shows absolute NLO QCD predictions. The lower panel presents differential  $\mathcal{K}$  factors. The CT14 PDF sets and  $\mu_0 = m_t + m_Z/2$  are employed.

different kinematical constraints, there is no physical way to distinguish them at the LHC and one must consider all of them under the total missing transverse momentum  $p_T^{miss}$ .

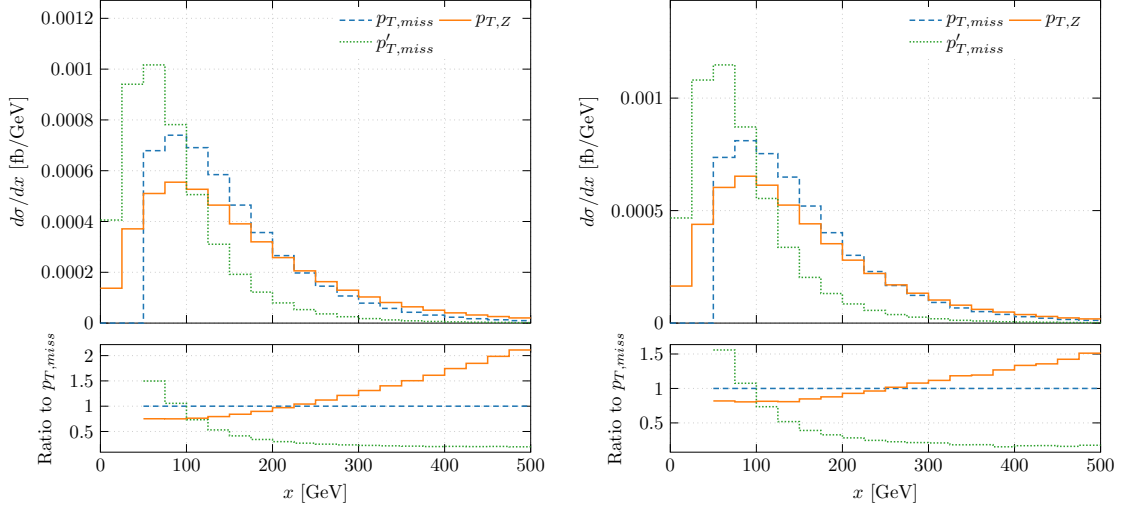


**Figure 11.** The  $pp \rightarrow e^+ \nu_e \mu^- \bar{\nu}_\mu b \bar{b} \nu_\tau \bar{\nu}_\tau + X$  LO (left panel) and NLO (right panel) differential cross section distribution as a function of  $p_T^{miss}$ ,  $p_{T,Z}$  and  $p_T^{miss}$  at the LHC run II with  $\sqrt{s} = 13$  TeV. The upper plots show absolute QCD predictions. The lower panels present ratios to  $p_T^{miss}$ . The CT14 PDF sets and  $\mu_0 = m_t + m_Z/2$  are employed.

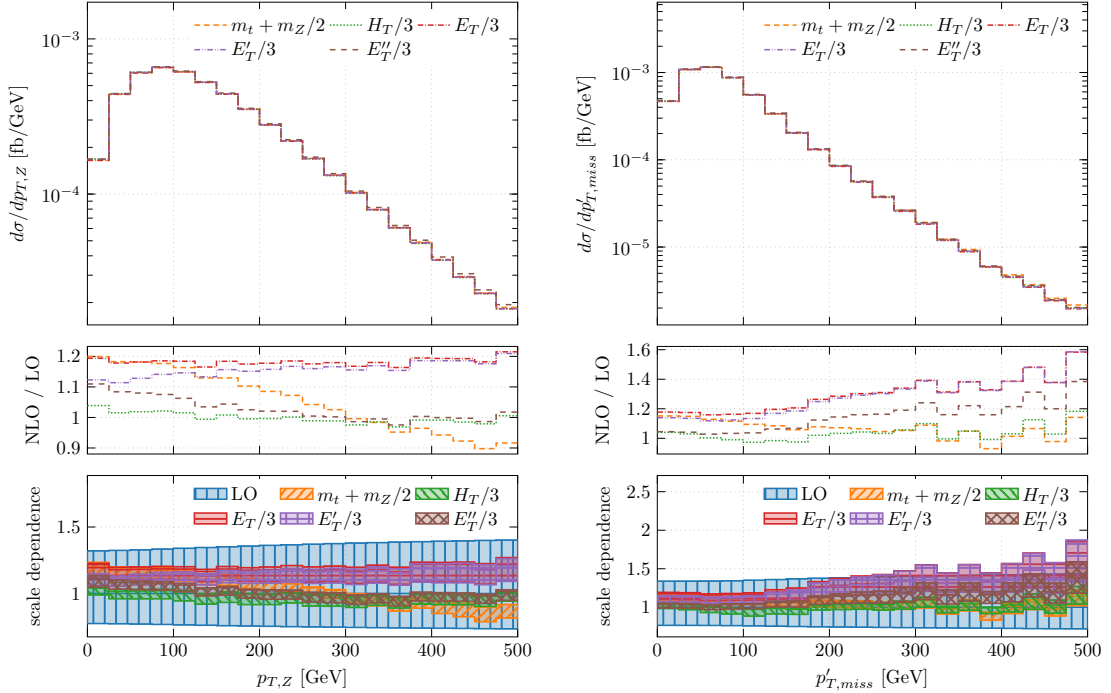


**Figure 12.** The  $pp \rightarrow e^+ \nu_e \mu^- \bar{\nu}_\mu b \bar{b} \nu_\tau \bar{\nu}_\tau + X$  differential cross section distribution as a function of  $p_{T,Z}$  and  $p_T^{miss}$  at the LHC run II with  $\sqrt{s} = 13$  TeV. The upper plots show absolute NLO QCD predictions for various values of  $\mu_0$  where  $\mu_R = \mu_F = \mu_0$ . The middle panels display differential  $\mathcal{K}$  factors. The lower panels present differential  $\mathcal{K}$  factors together with the uncertainty band from the scale variation for various values of  $\mu_0$ . Also given is the relative scale uncertainties of the LO cross section for  $\mu_0 = m_t + m_Z/2$ . The LO and the NLO CT14 PDF sets are employed.

The NLO differential cross section as a function of  $p_T^{miss}$  is shown in Figure 9. We observe substantial NLO QCD corrections when our recommended scale choice, based either

on  $\mu_0 = H_T/3$  or  $\mu_0 = E_T''/3$ , is employed. Such corrections are positive and amount respectively to 57% and 48% at the end of the plotted spectrum, i.e. for  $p_T^{miss} \approx 500$  GeV. We also observe that such corrections induce severe shape distortions in the  $p_T^{miss}$  distribution, of the order of 71% for  $\mu_0 = H_T/3$  and 51% for  $\mu_0 = E_T''/3$ . Comparing with the fixed scale predictions based on the choice  $\mu_0 = m_t + m_Z/2$ , one can see that the latter behaves much better. Specifically, in the region  $p_T^{miss} \approx 500$  GeV the NLO QCD corrections amount to 27% and shape distortions up to 19%. This behaviour contrasts with the behaviour for other observables, where the dynamical scale choice has been shown to guarantee reduced shape distortions.

In the attempt to understand why the fixed scale choice performs better for the  $p_T^{miss}$  observable we analyse the double differential NLO cross section distribution expressed as a function of  $p_T^{miss}$  and  $m_{t\bar{t}}$ , see Figure 10. One expects that the fixed scale choice performs well whenever the phase space regions close to the  $t\bar{t}$  threshold ( $m_{t\bar{t}} \approx 2m_t$ ) provide the dominant contribution to the observable under consideration. However, Figure 10 shows that this is not the case for  $p_T^{miss}$ . Not only the region with  $m_{t\bar{t}} \approx 2m_t$  is not enhanced in any special way, but the contributions to  $p_T^{miss}$ , which have the largest impact come from regions far away from the threshold, especially for  $p_T^{miss} \in [400 - 500]$  GeV.

Having established that the threshold region is not responsible for the better performance of the scale choice  $\mu_0 = m_t + m_Z/2$ , we move to another possible explanation. To this end we investigate two additional observables:

$$p_{T,Z} = |\vec{p}_{T,\nu_\tau} + \vec{p}_{T,\bar{\nu}_\tau}|, \quad p_T^{\prime miss} = |\vec{p}_{T,\nu_e} + \vec{p}_{T,\bar{\nu}_\mu}|. \quad (4.5)$$

Although not directly measurable at the LHC, these could help us to understand the different behaviour of  $p_T^{miss}$  under fixed and dynamical scale choices. The first one  $p_{T,Z}$ , corresponds to the transverse momentum of the  $Z$  boson reconstructed from its invisible decay products ( $Z \rightarrow \nu_\tau \bar{\nu}_\tau$ ). The second one  $p_T^{\prime miss}$  represents the missing transverse momentum restricted to the invisible particles coming from the decays of the top quarks only ( $t \rightarrow e^+ \nu_e b$  and  $\bar{t} \rightarrow \mu^- \bar{\nu}_\mu \bar{b}$ ). Given the different origin of the neutrinos involved in their definition, it is not surprising that these two observables exhibit different kinematics. Moreover, one should not expect that they are affected by higher order corrections in a similar way. We also note that the total missing transverse momentum,  $p_T^{miss}$ , is not given as a simple sum of  $p_{T,Z}$  and  $p_T^{\prime miss}$  but rather as a convolution of some type. In Figure 11 we present a comparison of LO and NLO differential cross section as a function of  $p_T^{miss}$ ,  $p_{T,Z}$  and  $p_T^{\prime miss}$  based on the fixed scale choice  $\mu_0 = m_t + m_Z/2$ , with the goal of outlining possible differences in kinematics. We are interested in regions above the  $p_T^{miss}$  cut of 50 GeV even though both  $p_{T,Z}$  and  $p_T^{\prime miss}$  can have lower values. One can observe that the  $p_T^{miss}$  spectrum is harder than  $p_T^{\prime miss}$ , but softer than  $p_{T,Z}$ . Additionally, shape differences between  $p_T^{miss}$  and  $p_{T,Z}$  are quite substantial. Figure 12 shows that  $p_{T,Z}$  and  $p_T^{\prime miss}$  are affected by NLO QCD corrections in a different way. In the case of  $p_{T,Z}$  the dynamical scale choice  $\mu_0 = H_T/3$  and  $\mu_0 = E_T''/3$  result in negative and rather small corrections of the order of 1% – 2% in the tail of the distribution. On the other hand, for the fixed scale choice we observe negative corrections of 8% in the same region. Dynamical scales feature also reduced shape distortions in comparison with the fixed scale (3% for  $\mu_0 = H_T/3$ , 9% for  $\mu_0 = E_T''/3$  and 28% for  $\mu_0 = m_t + m_Z/2$ ). A different pattern reveals itself when we turn to the case of  $p_T^{\prime miss}$ . In this case the dynamical scales result in sizeable NLO QCD corrections in the tail of the distribution (18% for  $\mu_0 = H_T/3$  and 38% for  $\mu_0 = E_T''/3$ ) to

SCALE CHOICE	$\sigma_{\text{CT14}}^{\text{NLO}}$ [fb]	$\sigma_{\text{MMHT2014}}^{\text{NLO}}$ [fb]	$\sigma_{\text{NNPDF3.0}}^{\text{NLO}}$ [fb]
$\mu_0 = m_t + m_Z/2$	$0.1266^{+0.0014(1.1\%)}_{-0.0075(5.9\%)}$	$0.1275^{+0.0014(1.1\%)}_{-0.0076(5.9\%)}$	$0.1309^{+0.0014(1.1\%)}_{-0.0079(6.0\%)}$
$\mu_0 = H_T/3$	$0.1270^{+0.0009(0.7\%)}_{-0.0086(6.8\%)}$	$0.1278^{+0.0009(0.7\%)}_{-0.0089(7.0\%)}$	$0.1312^{+0.0009(0.7\%)}_{-0.0090(6.9\%)}$
$\mu_0 = E_T/3$	$0.1272^{+0.0020(1.6\%)}_{-0.0086(6.8\%)}$	$0.1279^{+0.0020(1.6\%)}_{-0.0086(6.8\%)}$	$0.1313^{+0.0021(1.6\%)}_{-0.0090(6.9\%)}$
$\mu_0 = E'_T/3$	$0.1268^{+0.0019(1.5\%)}_{-0.0081(6.4\%)}$	$0.1280^{+0.0019(1.5\%)}_{-0.0082(6.4\%)}$	$0.1315^{+0.0020(1.5\%)}_{-0.0086(6.5\%)}$
$\mu_0 = E''_T/3$	$0.1286^{+0.0013(1.0\%)}_{-0.0060(4.7\%)}$	$0.1295^{+0.0013(1.0\%)}_{-0.0060(4.7\%)}$	$0.1330^{+0.0013(1.0\%)}_{-0.0063(4.8\%)}$

**Table 4.** *NLO cross sections for the  $pp \rightarrow e^+ \nu_e \mu^- \bar{\nu}_\mu b \bar{b} \nu_\tau \bar{\nu}_\tau + X$  process at the LHC run II with  $\sqrt{s} = 13$  TeV. Results for three different PDF sets are presented. Also included are theoretical errors as obtained from the scale variation.*

be compared with the more satisfactory performance of the fixed scale (14%). Moreover, the fixed scale choice provides negligible shape distortions in the tail of the order of 1%. Thus, like for  $p_T^{\text{miss}}$  also for  $p_T^{\prime\text{miss}}$  the scale  $\mu_0 = m_t + m_Z/2$  seems to perform better.

To conclude, our differential analysis of  $p_T^{\text{miss}}$ ,  $p_T^{\prime\text{miss}}$  and  $p_{T,Z}$  reveals that the first two observables have spectra which are much softer than the one of  $p_{T,Z}$ . For the latter, as well as for other dimensionful observables that we have studied in this paper, the prescription of using a dynamical scale seems the most adequate to describe the high  $p_T$  tails. Instead, for  $p_T^{\text{miss}}$  as well as for  $p_T^{\prime\text{miss}}$  such prescription results in too large scales. In this case a fixed scale choice is simply more adequate.

To close this part, we report on the size of the theoretical error as derived from the scale dependence study. In the case of  $p_T^{\text{miss}}$  for  $\mu_0 = m_t + m_Z/2$  the theoretical uncertainties are up to  $\pm 14\%$  ( $\pm 12\%$ ). They are slightly increased for our chosen dynamical scales up to  $\pm 18\%$  ( $\pm 17\%$ ). As usual the values in parenthesis correspond to the theoretical errors after the symmetrisation of errors is performed. This is of course a significant reduction in the theoretical error considering that at the LO one can obtain errors up to  $\pm 43\%$  ( $\pm 36\%$ ). Even though  $p_T^{\text{miss}}$  and  $p_{T,Z}$  can not be separately measured at the LHC we give theoretical errors for them as well for completeness. Specifically, for the former observable we have estimated errors up to  $\pm 11\%$  ( $\pm 9\%$ ) and for the latter we have received  $\pm 11\%$  ( $\pm 5\%$ ) with  $\mu_R = \mu_F = \mu_0$  set to  $\mu_0 = m_t + m_Z/2$ . The dynamical scale choices have left us with a theoretical error of the order of  $\pm 15\%$  ( $\pm 15\%$ ) and  $\pm 7\%$  ( $\pm 4\%$ ) respectively for  $p_T^{\prime\text{miss}}$  and  $p_{T,Z}$ . Once more, there is a significant improvement when comparing to the LO results where such errors have been estimated to be up to  $\pm 45\%$  ( $\pm 37\%$ ) and  $\pm 42\%$  ( $\pm 34\%$ ) respectively for  $p_T^{\prime\text{miss}}$  and  $p_{T,Z}$ .

#### 4.6 PDF uncertainties

In this section, we complete our analysis of theoretical uncertainties. The theoretical uncertainty as obtained from the scale dependence of the cross section is not the only source of theoretical systematic uncertainties. Another source of uncertainties comes from the parameterisation of PDFs. In the following we take the PDF uncertainties to be the difference between our default PDF set (CT14) and the other two PDF sets considered (MMHT14 and NNPDF3.0). In this way we account for different theoretical assumptions that enter into

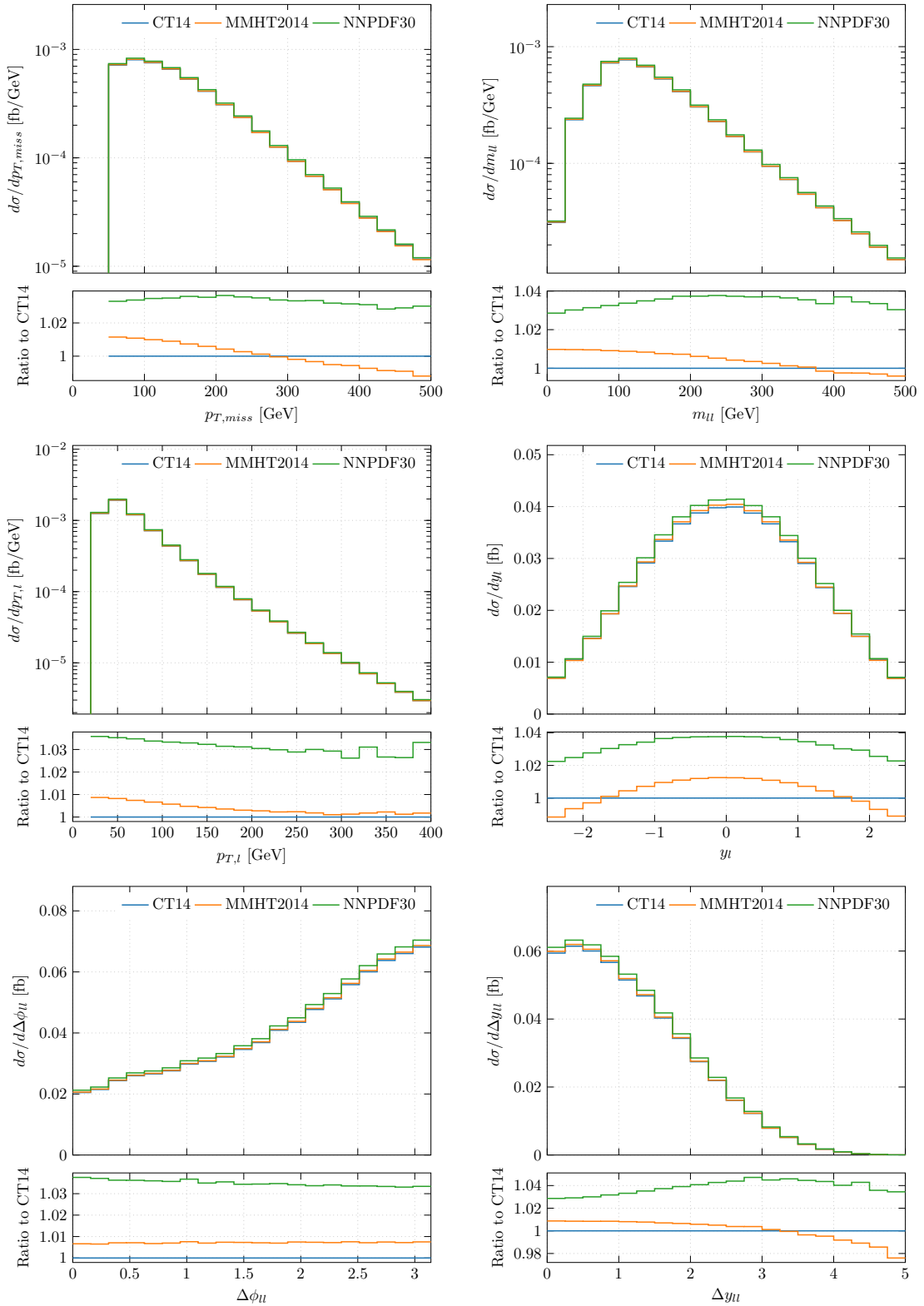


**Figure 13.** Differential cross section distributions for  $pp \rightarrow e^+ \nu_e \mu^- \bar{\nu}_\mu b \bar{b} \nu_\tau \bar{\nu}_\tau + X$  at the LHC run II with  $\sqrt{s} = 13$  TeV. The upper plots show absolute NLO QCD predictions for three different PDF sets and for  $\mu_0 = H_T/3$ . Lower panels display the ratio to the default CT14 set. The following observables are presented:  $p_T^{miss}$ ,  $m_{\ell\ell}$ , (averaged)  $p_{T,\ell}$ , (averaged)  $y_\ell$  as well as  $\Delta\phi_{\ell\ell}$  and  $\Delta y_{\ell\ell}$ .

the parameterisation of the PDFs which are difficult to quantify within the CT14 scheme. Moreover, the differences coming from NLO results for various PDF sets are comparable (usually even higher) to the individual estimates of PDF systematics. We have checked that this is the case for similar processes, namely for  $pp \rightarrow e^+ \nu_e \mu^- \bar{\nu}_\mu \bar{b} \bar{b} j + X$  [43, 44] and  $pp \rightarrow e^+ \nu_e \mu^- \bar{\nu}_\mu \bar{b} \bar{b} \gamma + X$  production [45, 60]. Results with the recomputed NLO QCD corrections to the  $pp \rightarrow e^+ \nu_e \mu^- \bar{\nu}_\tau \bar{b} \bar{b} \nu_\tau \bar{\nu}_\tau + X$  production process for MMHT14 and NNPDF3.0 PDF sets are summarised in Table 4. Taken in a very conservative way, the PDF uncertainties for the process under scrutiny and with  $\mu_R = \mu_F = \mu_0 = m_t + m_Z/2$  are of the order of 0.0043 fb (3.4%). After symmetrisation they are reduced down to 0.0026 fb (2.0%). Our result for the integrated cross section at NLO in QCD with the CT14 PDF set and for  $\mu_0 = m_t + m_Z/2$  is, thus, given by

$$\sigma_{pp \rightarrow e^+ \nu_e \mu^- \bar{\nu}_\mu \bar{b} \bar{b} \nu_\tau \bar{\nu}_\tau}^{\text{NLO}}(\mu_0 = m_t + m_Z/2) = 0.1266_{-0.0075(5.9\%)}^{+0.0014(1.1\%)} [\text{scales}]_{+0.0043(3.4\%)}^{+0.0009(0.7\%)} [\text{PDF}] \text{ fb}. \quad (4.6)$$

The PDF uncertainties are almost a factor of 2 smaller than the theoretical uncertainties due to the scale dependence. The latter remain the dominant source of the theoretical systematics. The same pattern is obtained for the other scale choices. For example for  $\mu_0 = H_T/3$  and  $\mu_0 = E_T''/3$  we have

$$\begin{aligned} \sigma_{pp \rightarrow e^+ \nu_e \mu^- \bar{\nu}_\mu \bar{b} \bar{b} \nu_\tau \bar{\nu}_\tau}^{\text{NLO}}(\mu_0 = H_T/3) &= 0.1270_{-0.0086(6.8\%)}^{+0.0009(0.7\%)} [\text{scales}]_{+0.0042(3.3\%)}^{+0.0008(0.6\%)} [\text{PDF}] \text{ fb}, \\ \sigma_{pp \rightarrow e^+ \nu_e \mu^- \bar{\nu}_\mu \bar{b} \bar{b} \nu_\tau \bar{\nu}_\tau}^{\text{NLO}}(\mu_0 = E_T''/3) &= 0.1286_{-0.0060(4.7\%)}^{+0.0013(1.0\%)} [\text{scales}]_{+0.0044(3.4\%)}^{+0.0009(0.7\%)} [\text{PDF}] \text{ fb}. \end{aligned} \quad (4.7)$$

Lastly, we have examined PDF uncertainties for various differential cross sections. In Figure 13 NLO differential distributions as a function of  $p_T^{\text{miss}}$ ,  $m_{\ell\ell}$ , the averaged  $p_{T,\ell}$ , the averaged  $y_\ell$  as well as  $\Delta\phi_{\ell\ell}$  and  $\Delta y_{\ell\ell}$  are shown as examples. The upper panels present the NLO predictions for three different PDF sets at the central scale value  $\mu_R = \mu_F = \mu_0 = H_T/3$ . The lower panels of Figure 13 give the ratio of the MMHT14 (NNPDF3.0) PDF set to CT14. As we can observe for all observables shown the PDF uncertainties are at most at the level of 4%, thus, well below the uncertainties from the scale dependence. This result remains unchanged regardless of whether the observable was dimensionful or not and independent of the scale we have utilised.

To summarise this part, for  $pp \rightarrow e^+ \nu_e \mu^- \bar{\nu}_\mu \bar{b} \bar{b} \nu_\tau \bar{\nu}_\tau$  production at the LHC Run II with  $\sqrt{s} = 13$  TeV with the rather inclusive selection cuts that we have employed and input parameters used, the size of PDF uncertainties, both at the level of total and differential cross sections, is substantially smaller than the size of theoretical errors from the scale dependence. The latter remain the dominant component of the final theoretical error for our predictions at NLO in QCD.

## 5 Comparison to top anti-top pair production

From the experimental point of view both the  $pp \rightarrow e^+ \nu_e \mu^- \bar{\nu}_\mu \bar{b} \bar{b}$  and  $pp \rightarrow e^+ \nu_e \mu^- \bar{\nu}_\mu \bar{b} \bar{b} \nu_\tau \bar{\nu}_\tau$  production processes comprise the same final states, two charged leptons, two bottom flavoured jets and missing transverse momentum from undetected neutrinos. In the following we would like to compare these two processes in order to see the impact of the enlarged missing transverse momentum on the kinematics of these final state. We start, however, by presenting the results for the integrated cross sections for the  $pp \rightarrow e^+ \nu_e \mu^- \bar{\nu}_\mu \bar{b} \bar{b}$

production process. With our inclusive cut selection LO predictions for two different scale choices  $\mu_0 = m_t/2$  and  $\mu_0 = H_T/4$  as well as for the CT14 PDF set are

$$\begin{aligned}\sigma_{pp \rightarrow e^+ \nu_e \mu^- \bar{\nu}_\mu b \bar{b}}^{\text{LO}}(\text{CT14}, \mu_0 = m_t/2) &= 1126_{-265}^{+379} (34\%) \text{ fb}, \\ \sigma_{pp \rightarrow e^+ \nu_e \mu^- \bar{\nu}_\mu b \bar{b}}^{\text{LO}}(\text{CT14}, \mu_0 = H_T/4) &= 1067_{-247}^{+348} (33\%) \text{ fb}.\end{aligned}\tag{5.1}$$

At the NLO level in QCD they are given by

$$\begin{aligned}\sigma_{pp \rightarrow e^+ \nu_e \mu^- \bar{\nu}_\mu b \bar{b}}^{\text{NLO}}(\text{CT14}, \mu_0 = m_t/2) &= 1107_{-88}^{+16} (1.4\%) \text{ fb}, \\ \sigma_{pp \rightarrow e^+ \nu_e \mu^- \bar{\nu}_\mu b \bar{b}}^{\text{NLO}}(\text{CT14}, \mu_0 = H_T/4) &= 1103_{-58}^{+19} (1.7\%) \text{ fb}.\end{aligned}\tag{5.2}$$

Since also in this case we generate decays of the weak bosons to different lepton generations only the complete  $\ell^\pm \ell^\mp$  cross section (with  $\ell_{1,2} = e, \mu$ ) can be obtained by multiplying the above result with a lepton-flavour factor of 4.

We observe that the integrated cross section for top quark pair production in the di-lepton top quark decay channel is 4 orders of magnitude larger than the one for  $pp \rightarrow e^+ \nu_e \mu^- \bar{\nu}_\mu b \bar{b} \nu_\tau \bar{\nu}_\tau$ . As already mentioned typical new physics scenarios predict cross sections for  $\ell^\pm \ell^\mp b \bar{b} + p_T^{\text{miss}}$  that are of the order of femtobarns. Thus, very exclusive and sophisticated cuts have to be employed to reduce the size of the reducible top quark background process keeping a sizeable amount of signal events at the same time. Such cut selection, that are designed to diminish the double and single top quark resonance contributions, would enhance the  $W^+ W^- b \bar{b}$  part in both  $t\bar{t}$  and  $t\bar{t}Z$  background processes. Moreover, the signal is expected to be a subtle excess over the SM backgrounds in the tails of kinematic variables, e.g. in the invariant mass of two charged leptons  $m_{\ell\ell}$ . Furthermore, shape differences in differential cross sections between signal and background processes can potentially be exploited to increase the signal to background ratio. Therefore, a proper modelling of top quark decays, including QCD effects in the top quark decay chain and incorporating the complete off-shell effects of the top quark, is simply mandatory.

In the following we concentrate on shape differences between the two main background processes  $pp \rightarrow e^+ \nu_e \mu^- \bar{\nu}_\mu b \bar{b}$  and  $pp \rightarrow e^+ \nu_e \mu^- \bar{\nu}_\mu b \bar{b} \nu_\tau \bar{\nu}_\tau$ . To this end in Figure 14 normalised differential distributions constructed from final states for both  $pp \rightarrow e^+ \nu_e \mu^- \bar{\nu}_\mu b \bar{b}$  and  $pp \rightarrow e^+ \nu_e \mu^- \bar{\nu}_\mu b \bar{b} \nu_\tau \bar{\nu}_\tau$  are depicted. They are given at NLO in QCD for the CT14 PDF set and for the dynamical scale choice. Specifically, for the  $pp \rightarrow e^+ \nu_e \mu^- \bar{\nu}_\mu b \bar{b} \nu_\tau \bar{\nu}_\tau$  process  $\mu_R = \mu_F = \mu_0 = H_T/3$  is used and for  $pp \rightarrow e^+ \nu_e \mu^- \bar{\nu}_\mu b \bar{b}$  the scale choice  $\mu_0 = H_T/4$  is utilised instead. For the total missing transverse momentum we notice large differences between the two background processes. Assuming for example, that it would be sufficient to consider the  $t\bar{t}$  background only in new physics analyses in the  $t\bar{t} + p_T^{\text{miss}}$  channel is not satisfactory or acceptable. We can observe that the  $p_T^{\text{miss}}$  observable, which is always employed to suppress the top-like backgrounds, has a harder missing  $p_T$  spectrum for  $e^+ \nu_e \mu^- \bar{\nu}_\mu b \bar{b} \nu_\tau \bar{\nu}_\tau$  than in the case of the  $e^+ \nu_e \mu^- \bar{\nu}_\mu b \bar{b}$  background. In the latter case  $p_T^{\text{miss}}$  is highly peaked towards low values. In the former case the primary source of the long  $p_T^{\text{miss}}$  tail is the neutrinos from the  $Z$  gauge boson decay. Because the  $pp \rightarrow e^+ \nu_e \mu^- \bar{\nu}_\mu b \bar{b}$  production process does not exhibit long enough tails in the  $p_T^{\text{miss}}$  distribution any final  $S/B$  ratios as calculated with the help of  $pp \rightarrow e^+ \nu_e \mu^- \bar{\nu}_\mu b \bar{b}$  only can be grossly overestimated. Consequently, limits on the signal strengths, which are usually translated into constraints on the parameter space of new physics models, might not be realistic.

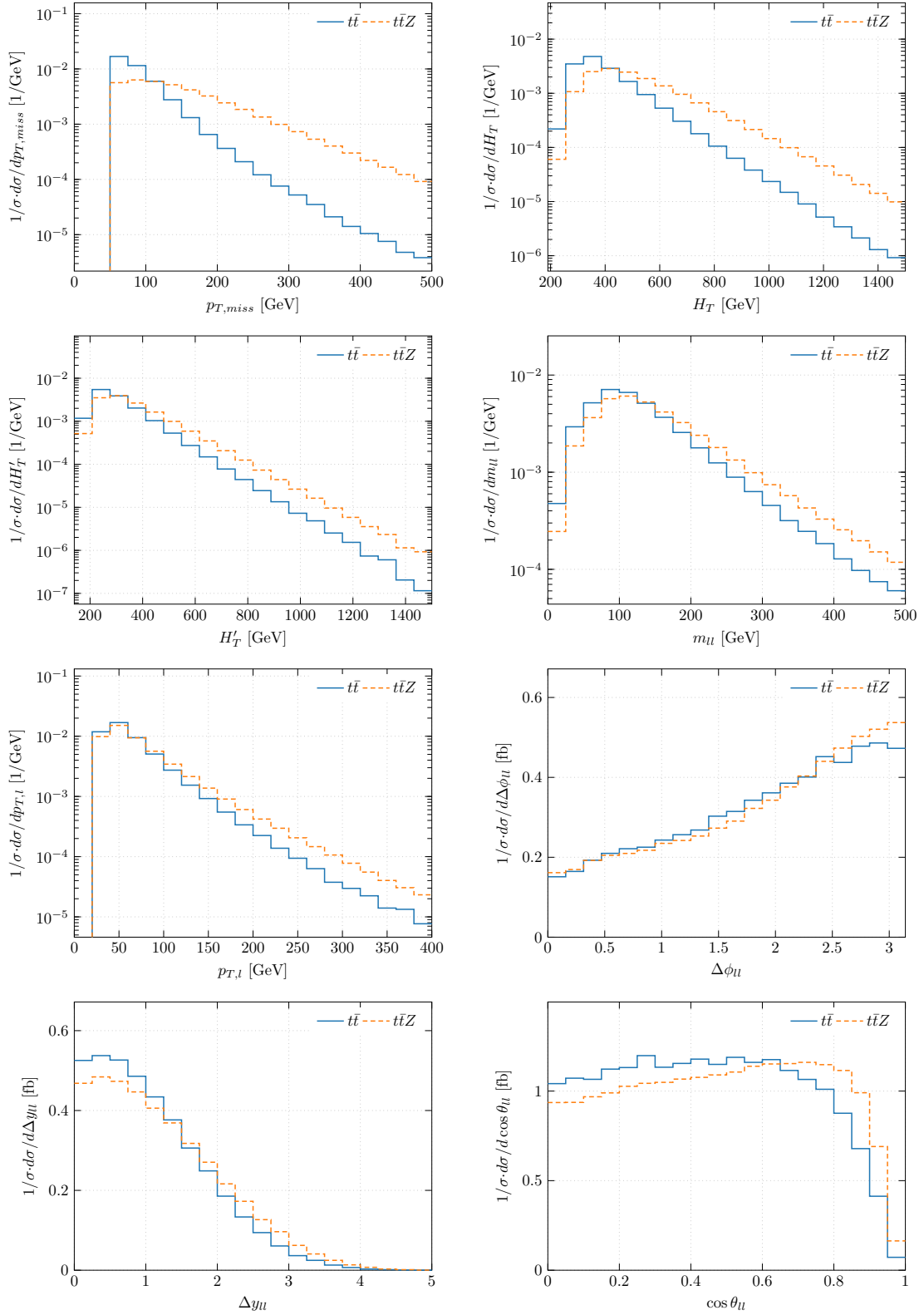


**Figure 14.** Comparison of the normalised NLO differential cross sections for  $pp \rightarrow e^+ \nu_e \mu^- \bar{\nu}_\mu b \bar{b} + X$  and  $pp \rightarrow e^+ \nu_e \mu^- \bar{\nu}_\mu b \bar{b} \nu_\tau \bar{\nu}_\tau + X$  at the LHC with  $\sqrt{s} = 13$  TeV. The following distributions are shown:  $p_T^{miss}$ ,  $H_T$ ,  $H_T'$ ,  $m_{\ell\ell}$ , (averaged)  $p_{T,\ell}$ ,  $\Delta\phi_{\ell\ell}$ ,  $\Delta y_{\ell\ell}$  and  $\cos\theta_{\ell\ell}$ . The NLO CT14 PDF set is employed and the scale choices  $\mu_0 = H_T/3$  ( $t\bar{t}Z$ ) and  $\mu_0 = H_T/4$  ( $t\bar{t}$ ) are utilised.

Large shape differences are also visible in the case of  $H_T$ , which is not surprising since  $p_T^{miss}$  is incorporated in the definition of the observable. We can further notice, however, that the shape of various observables built out of the charged leptons and  $b$ -jets only, i.e. out of visible final states, have been changed by the enlarged  $p_T^{miss}$ . Shape differences can be noticed both for dimensionful and dimensionless observables. In the case of  $H_T'$ ,  $m_{\ell\ell}$  and the (averaged) transverse momentum of the charged lepton,  $p_{T,\ell}$  the spectra are harder when the additional contribution to  $p_T^{miss}$  is included. In the case of dimensionless observables we depict  $\Delta\phi_{\ell\ell}$ ,  $\Delta y_{\ell\ell}$  and  $\cos\theta_{\ell\ell}$  where shape differences are the most pronounced and visible over the whole plotted range. Let us say again at this point that both  $H_T$  and  $H_T'$  are very often used to further suppress reducible top quark backgrounds in new physics analyses, whereas  $\Delta\phi_{\ell\ell}$ ,  $\Delta y_{\ell\ell}$  and  $\cos\theta_{\ell\ell}$  are regularly employed either to enhance sensitivity of the new physics signal or to verify the hypothesis of scalar/vector nature of the new heavy resonances that are associated with various BSM hypothesis. Consequently, the  $pp \rightarrow \nu_e\mu^-\bar{\nu}_\mu b\bar{b}\nu_\tau\bar{\nu}_\tau$  irreducible background process has to be always taken into account and carefully studied for the proper description of relevant observables in the  $t\bar{t} + p_T^{miss}$  channel.

## 6 Summary and Conclusions

In this paper, we have presented the first complete NLO QCD prediction for the  $pp \rightarrow t\bar{t}Z(\rightarrow \nu_\tau\bar{\nu}_\tau)$  process in the di-lepton top quark decay channel for the LHC run II energy of  $\sqrt{s} = 13$  TeV. With an inclusive cut selection and for  $\mu_R = \mu_F = \mu_0 = m_t + m_Z/2$  NLO QCD corrections reduce the unphysical scale dependence by a factor of 6 (8 after symmetrisation of errors) and increase the total rate by about 12% compared to the LO prediction. The theoretical uncertainty of the NLO cross section as estimated from scale dependence is 5.9% (3.5% after symmetrisation). By comparison, the PDF uncertainties are negligible. Taken in a very conservative way, they are of the order of 3.4%. After symmetrisation, they are reduced down to 2.0%. Consequently, the theoretical uncertainty resulting from the scale variation remains the dominant source of theoretical systematics.

Similar conclusions can be drawn from the results with  $\mu_0 = H_T/3$  and  $\mu_0 = E_T''/3$ . Specifically, NLO QCD corrections of the order of 1% and 5% have been obtained respectively for  $\mu_0 = H_T/3$  and  $\mu_0 = E_T''/3$ . Our best NLO QCD predictions for the  $pp \rightarrow e^+\nu_e\mu^-\bar{\nu}_\mu b\bar{b}\nu_\tau\bar{\nu}_\tau$  process can be summarised as

$$\begin{aligned} \sigma_{pp \rightarrow e^+\nu_e\mu^-\bar{\nu}_\mu b\bar{b}\nu_\tau\bar{\nu}_\tau}^{\text{NLO}}(\mu_0 = H_T/3) &= 0.1270_{-0.0086(6.8\%)}^{+0.0009(0.7\%)} [\text{scales}]_{+0.0042(3.3\%)}^{+0.0008(0.6\%)} [\text{PDF}] \text{ fb}, \\ \sigma_{pp \rightarrow e^+\nu_e\mu^-\bar{\nu}_\mu b\bar{b}\nu_\tau\bar{\nu}_\tau}^{\text{NLO}}(\mu_0 = E_T''/3) &= 0.1286_{-0.0060(4.7\%)}^{+0.0013(1.0\%)} [\text{scales}]_{+0.0044(3.4\%)}^{+0.0009(0.7\%)} [\text{PDF}] \text{ fb}. \end{aligned} \quad (6.1)$$

The complete cross section for  $pp \rightarrow \ell^+\nu_\ell\ell^-\bar{\nu}_\ell b\bar{b}\nu_\ell\bar{\nu}_\ell$ , where  $\ell = e, \mu$  and  $\nu_\ell = \nu_e, \nu_\mu, \nu_\tau$  can be obtained by multiplying the above results by 12. Despite the relatively small cross section, good theoretical control over the  $pp \rightarrow e^+\nu_e\mu^-\bar{\nu}_\mu b\bar{b}\nu_\tau\bar{\nu}_\tau$  production process is phenomenologically relevant. This irreducible SM background is of the order of 1.5 fb at NLO in QCD. For comparison, typical predictions for DM scenarios are also at a similar level.

In a next step, we examined the size of NLO QCD corrections to various differential distributions with the different scale choices that we have proposed. We started with standard observables that describe charged lepton and  $b$ -jet kinematics. We have thoroughly

investigated the following set of observables: (averaged)  $p_{T,\ell}$ ,  $m_{\ell\ell}$ , (averaged)  $y_\ell$  and  $\Delta R_{\ell\ell}$  as well as (averaged)  $p_{T,b}$ ,  $m_{b\bar{b}}$ , (averaged)  $y_b$  and  $\Delta R_{b\bar{b}}$ . Differential cross sections have shown large differences in shape with respect to LO within our fixed-scale setting, i.e. for  $\mu_0 = m_t + m_Z/2$ . In particular, large negative corrections have been clearly seen in the tails of several distributions for dimensionful observables. Thus, an accurate description of the shapes of observables can only be given via a full NLO QCD computation in this case. Adopting  $\mu_0 = H_T/3$  and  $\mu_0 = E_T''/3$  dynamical scale choices, resulted in moderate higher order QCD corrections up to 10%–15%. The NLO theoretical uncertainties for the leptonic and  $b$ -jet observables as estimated from scale variation were of the order of  $\pm 10\%$  ( $\pm 5\%$  after symmetrisation). Combining information about the size of NLO QCD corrections and the NLO QCD theoretical uncertainties, we concluded that either scale  $\mu_0 = H_T/3$  or  $\mu_0 = E_T''/3$  may be employed at the differential level for an adequate description of the standard observables in the  $e^+\nu_e\mu^-\bar{\nu}_\mu b\bar{b}\nu_\tau\bar{\nu}_\tau$  production process at the LHC with a centre of mass system energy of  $\sqrt{s} = 13$  TeV in the presence of rather inclusive cuts on the measured final states.

Moving forward, we employed our recommended dynamical scale choices to discuss the size of NLO QCD corrections to a few observables that are particularly relevant in the context of dark matter searches. Among others, we have identified six observables, three dimensionful  $E_T$ ,  $H_T$  and  $H_T'$  as well as three dimensionless  $\Delta y_{\ell\ell}$ ,  $\Delta\phi_{\ell\ell}$  and  $\cos\theta_{\ell\ell}$ . Substantial NLO QCD corrections up to 35% ( $\pm 20\%$ ) have been obtained for dimensionful (dimensionless) observables. Overall, the differential  $\mathcal{K}$ -factors show major changes in the shape of the observables. On the other hand, NLO QCD theoretical uncertainties up to  $\pm 20\%$  ( $\pm 10\%$ ) have been estimated from scale variation. Well behaved as they are at NLO in QCD, these leptonic observables can now be safely utilised to probe new physics at the LHC.

Among all infrared-safe observables in  $e^+\nu_e\mu^-\bar{\nu}_\mu b\bar{b}\nu_\tau\bar{\nu}_\tau$  production, the total missing transverse momentum plays a special role. The observation of an access in  $p_T^{miss}$  represents the most important signature in various BSM and DM models. Thus, we investigated this observable separately. We observed substantial NLO QCD corrections up to 57% and 48% when our recommended scale choice, based either on  $\mu_0 = H_T/3$  or  $\mu_0 = E_T''/3$ , was employed. Predictions based on the fixed scale choice  $\mu_0 = m_t + m_Z/2$ , however, received NLO QCD corrections up to 27% only and showed shape distortions up to 19%. This behaviour is to be contrasted with the behaviour for other observables, where the dynamical scale choice guaranteed reduced shape distortions. In order to understand why the fixed scale choice performed better for the  $p_T^{miss}$  observable, we analysed the double differential NLO cross section distribution expressed as a function of  $p_T^{miss}$  and  $m_{t\bar{t}}$ . Furthermore, we investigated two additional observables: the transverse momentum of the  $Z$  boson reconstructed from its invisible decay products ( $p_{T,Z}$ ) as well as the missing transverse momentum restricted to the invisible particles coming from the decays of the top quarks only ( $p_T'^{miss}$ ). Our differential analysis revealed that in the case of  $p_T^{miss}$  and  $p_T'^{miss}$  the proposed dynamic scale choices resulted in too large scales and the fixed scale choice was simply more adequate.

In a next step, we studied the theoretical uncertainty related to the parameterisation of PDFs. For all observables that we have scrutinised the PDF uncertainties have been substantially smaller than the theoretical uncertainties from the scale dependence. The latter remains the dominant source of the final theoretical error for our predictions at NLO

in QCD.

Finally, because  $pp \rightarrow e^+ \nu_e \mu^- \bar{\nu}_\mu b \bar{b}$  and  $pp \rightarrow e^+ \nu_e \mu^- \bar{\nu}_\mu b \bar{b} \nu_\tau \bar{\nu}_\tau$  comprise the same final states (two charged leptons, two bottom flavoured jets and missing transverse momentum from undetected neutrinos) we compared the two production processes to quantify the impact of the enlarged missing transverse momentum on the kinematics of the final state. Substantial shape differences have been observed both for dimensionful and dimensionless observables. Both kinds of observables have often been employed to enhance sensitivity of the new physics signal or to verify the hypothesis of scalar/vector nature of the new heavy resonances that are associated with various BSM hypotheses. For example, since the  $pp \rightarrow e^+ \nu_e \mu^- \bar{\nu}_\mu b \bar{b}$  production process does not exhibit long enough tails in the  $p_T^{miss}$  distribution, any final  $S/B$  ratios as calculated with the help of  $pp \rightarrow e^+ \nu_e \mu^- \bar{\nu}_\mu b \bar{b}$  only, can be grossly overestimated. As a result, limits on the signal strengths, which are usually translated into constraints on the parameter space of new physics models, might not be very realistic. Consequently, the  $pp \rightarrow \nu_e \mu^- \bar{\nu}_\mu b \bar{b} \nu_\tau \bar{\nu}_\tau$  irreducible background process must be additionally taken into account in searches of new physics in the  $t\bar{t} + p_T^{miss}$  channel. Good theoretical control over the irreducible SM background is, therefore, a fundamental prerequisite for a correct interpretation of possible signals of new physics that may arise in this channel.

On the technical side let us mention that all results have been generated with the help of the HELAC-NLO MC framework. The results are available as event files in the form of either LHEFs or ROOT Ntuples. These might be directly used for experimental analyses at the LHC as well as for obtaining accurate SM predictions in BSM studies. The Ntuple files are available upon request.

## Acknowledgments

The work of M.W. and T.W. was supported in part by the German Research Foundation (DFG) Individual Research Grant: "*Top-Quarks under the LHCs Magnifying Glass: From Process Modelling to Parameter Extraction*" and in part by the DFG Collaborative Research Centre/Transregio project CRC/TRR 257: "*P3H - Particle Physics Phenomenology after the Higgs Discovery*".

The work of H.B.H. has received funding from the European Research Council (ERC) under the European Union's Horizon 2020 research and innovation programme (grant agreement No 772099) and partial support from Rutherford Grant ST/M004104/1.

The research of G.B. was supported by grant K 125105 of the National Research, Development and Innovation Office in Hungary.

Support by a grant of the Bundesministerium für Bildung und Forschung (BMBF) is additionally acknowledged.

Simulations were performed with computing resources granted by RWTH Aachen University under project `rwth0414`.

## References

- [1] C. Arina *et al.*, *A comprehensive approach to dark matter studies: exploration of simplified top-philic models*, JHEP **1611** (2016) 111 [[arXiv:1605.09242](#) [[hep-ph](#)]].

- [2] G. D’Ambrosio, G. F. Giudice, G. Isidori and A. Strumia, *Minimal flavor violation: An Effective field theory approach*, Nucl. Phys. B **645** (2002) 155, [[hep-ph/0207036](#)].
- [3] G. Aad *et al.* [ATLAS Collaboration], *Search for dark matter in events with heavy quarks and missing transverse momentum in pp collisions with the ATLAS detector*, Eur. Phys. J. C **75** (2015) no.2, 92 [[arXiv:1410.4031](#) [[hep-ex](#)]].
- [4] V. Khachatryan *et al.* [CMS Collaboration], *Search for the production of dark matter in association with top-quark pairs in the single-lepton final state in proton-proton collisions at  $\sqrt{s} = 8$  TeV*, JHEP **1506** (2015) 121 [[arXiv:1504.03198](#) [[hep-ex](#)]].
- [5] A. M. Sirunyan *et al.* [CMS Collaboration], *Search for dark matter produced in association with heavy-flavor quark pairs in proton-proton collisions at  $\sqrt{s} = 13$  TeV*, Eur. Phys. J. C **77** (2017) no.12, 845 [[arXiv:1706.02581](#) [[hep-ex](#)]].
- [6] M. Aaboud *et al.* [ATLAS Collaboration], *Search for direct top squark pair production in final states with two leptons in  $\sqrt{s} = 13$  TeV pp collisions with the ATLAS detector*, Eur. Phys. J. C **77** (2017) no.12, 898 [[arXiv:1708.03247](#) [[hep-ex](#)]].
- [7] M. Aaboud *et al.* [ATLAS Collaboration], *Search for dark matter produced in association with bottom or top quarks in  $\sqrt{s} = 13$  TeV pp collisions with the ATLAS detector*, Eur. Phys. J. C **78** (2018) no.1, 18 [[arXiv:1710.11412](#) [[hep-ex](#)]].
- [8] A. M. Sirunyan *et al.* [CMS Collaboration], *Search for top squarks and dark matter particles in opposite-charge dilepton final states at  $\sqrt{s} = 13$  TeV*, Phys. Rev. D **97** (2018) no.3, 032009 [[arXiv:1711.00752](#) [[hep-ex](#)]].
- [9] A. M. Sirunyan *et al.* [CMS Collaboration], *Inclusive search for supersymmetry in pp collisions at  $\sqrt{s} = 13$  TeV using razor variables and boosted object identification in zero and one lepton final states*, JHEP **1903** (2019) 031 [[arXiv:1812.06302](#) [[hep-ex](#)]].
- [10] A. M. Sirunyan *et al.* [CMS Collaboration], *Search for dark matter produced in association with a single top quark or a top quark pair in proton-proton collisions at  $\sqrt{s} = 13$  TeV*, JHEP **1903** (2019) 141 [[arXiv:1901.01553](#) [[hep-ex](#)]].
- [11] K. Cheung, K. Mawatari, E. Senaha, P. Y. Tseng and T. C. Yuan, *The Top Window for dark matter*, JHEP **1010** (2010) 081 [[arXiv:1009.0618](#) [[hep-ph](#)]].
- [12] T. Lin, E. W. Kolb and L. T. Wang, *Probing dark matter couplings to top and bottom quarks at the LHC*, Phys. Rev. D **88** (2013) no.6, 063510 [[arXiv:1303.6638](#) [[hep-ph](#)]].
- [13] U. Haisch and E. Re, *Simplified dark matter top-quark interactions at the LHC*, JHEP **1506** (2015) 078 [[arXiv:1503.00691](#) [[hep-ph](#)]].
- [14] U. Haisch, P. Pani and G. Polesello, *Determining the CP nature of spin-0 mediators in associated production of dark matter and  $t\bar{t}$  pairs*, JHEP **1702** (2017) 131 [[arXiv:1611.09841](#) [[hep-ph](#)]].
- [15] Y. Bai, H. C. Cheng, J. Gallicchio and J. Gu, *Stop the Top Background of the Stop Search*, JHEP **1207** (2012) 110 [[arXiv:1203.4813](#) [[hep-ph](#)]].
- [16] A. Lazopoulos, T. McElmurry, K. Melnikov and F. Petriello, *Next-to-leading order QCD corrections to  $t\bar{t}Z$  production at the LHC*, Phys. Lett. B **666** (2008) 62 [[arXiv:0804.2220](#) [[hep-ph](#)]].
- [17] A. Kardos, Z. Trocsanyi and C. Papadopoulos, *Top quark pair production in association with a Z-boson at NLO accuracy*, Phys. Rev. D **85** (2012) 054015 [[arXiv:1111.0610](#) [[hep-ph](#)]].
- [18] M. V. Garzelli, A. Kardos, C. G. Papadopoulos and Z. Trocsanyi,  *$Z^0$  - boson production in association with a top anti-top pair at NLO accuracy with parton shower effects* Phys. Rev. D **85** (2012) 074022 [[arXiv:1111.1444](#) [[hep-ph](#)]].

- [19] M. V. Garzelli, A. Kardos, C. G. Papadopoulos and Z. Trocsanyi,  *$t\bar{t}W^\pm$  and  $t\bar{t}Z$  Hadroproduction at NLO accuracy in QCD with Parton Shower and Hadronization effects*, JHEP **1211** (2012) 056 [[arXiv:1208.2665](#) [[hep-ph](#)]].
- [20] O. Bessidskaia Bylund, F. Maltoni, I. Tsinikos, E. Vryonidou and C. Zhang, *Probing top quark neutral couplings in the Standard Model Effective Field Theory at NLO in QCD*, JHEP **1605** (2016) 052 [[arXiv:1601.08193](#) [[hep-ph](#)]].
- [21] R. Röntsch and M. Schulze, *Constraining couplings of top quarks to the Z boson in  $t\bar{t} + Z$  production at the LHC*, JHEP **1407** (2014) 091 Erratum: [JHEP **1509** (2015) 132] [[arXiv:1404.1005](#) [[hep-ph](#)]].
- [22] S. Frixione, V. Hirschi, D. Pagani, H.-S. Shao and M. Zaro, *Electroweak and QCD corrections to top-pair hadroproduction in association with heavy bosons*, JHEP **1506** (2015) 184 [[arXiv:1504.03446](#) [[hep-ph](#)]].
- [23] A. Kulesza, L. Motyka, D. Schwartländer, T. Stebel and V. Theeuwes, *Associated production of a top quark pair with a heavy electroweak gauge boson at NLO+NNLL accuracy*, Eur. Phys. J. C **79** (2019) no.3, 249 [[arXiv:1812.08622](#) [[hep-ph](#)]].
- [24] A. Broggio, A. Ferroglia, G. Ossola, B. D. Pecjak and R. D. Sameshima, *Associated production of a top pair and a Z boson at the LHC to NNLL accuracy*, JHEP **1704** (2017) 105 [[arXiv:1702.00800](#) [[hep-ph](#)]].
- [25] M. Czakon, C. G. Papadopoulos and M. Worek, *Polarizing the Dipoles*, JHEP **0908** (2009) 085 [[arXiv:0905.0883](#) [[hep-ph](#)]].
- [26] A. Cafarella, C. G. Papadopoulos and M. Worek, *Helac-Phegas: A Generator for all parton level processes*, Comput. Phys. Commun. **180** (2009) 1941 [[arXiv:0710.2427](#) [[hep-ph](#)]].
- [27] A. van Hameren, *PARNI for importance sampling and density estimation*, Acta Phys. Polon. B **40** (2009) 259 [[arXiv:0710.2448](#) [[hep-ph](#)]].
- [28] A. van Hameren, *Kaleu: A General-Purpose Parton-Level Phase Space Generator*, [arXiv:1003.4953](#) [[hep-ph](#)].
- [29] A. Denner, S. Dittmaier, M. Roth and D. Wackerth, *Predictions for all processes  $e^+e^- \rightarrow 4$  fermions +  $\gamma$* , Nucl. Phys. B **560** (1999) 33 [[hep-ph/9904472](#)].
- [30] A. Denner, S. Dittmaier, M. Roth and L. H. Wieders, *Electroweak corrections to charged-current  $e^+e^- \rightarrow 4$  fermion processes: Technical details and further results*, Nucl. Phys. B **724** (2005) 247 Erratum: [Nucl. Phys. B **854** (2012) 504] [[hep-ph/0505042](#)].
- [31] G. Bevilacqua, M. Czakon, A. van Hameren, C. G. Papadopoulos and M. Worek, *Complete off-shell effects in top quark pair hadroproduction with leptonic decay at next-to-leading order*, JHEP **1102** (2011) 083 [[arXiv:1012.4230](#) [[hep-ph](#)]].
- [32] A. Denner, S. Dittmaier, S. Kallweit and S. Pozzorini, *NLO QCD corrections to off-shell top-antitop production with leptonic decays at hadron colliders*, JHEP **1210** (2012) 110 [[arXiv:1207.5018](#) [[hep-ph](#)]].
- [33] P. Nogueira, *Automatic Feynman graph generation*, J. Comput. Phys. **105** (1993) 279.
- [34] J. Alwall *et al.*, *The automated computation of tree-level and next-to-leading order differential cross sections, and their matching to parton shower simulations*, JHEP **1407** (2014) 079 [[arXiv:1405.0301](#) [[hep-ph](#)]].
- [35] A. van Hameren, C. G. Papadopoulos and R. Pittau, *Automated one-loop calculations: A Proof of concept*, JHEP **0909** (2009) 106 [[arXiv:0903.4665](#) [[hep-ph](#)]].
- [36] G. Ossola, C. G. Papadopoulos and R. Pittau, *CutTools: A Program implementing the OPP*

- reduction method to compute one-loop amplitudes, JHEP **0803** (2008) 042 [[arXiv:0711.3596](#) [[hep-ph](#)]].
- [37] A. van Hameren, *OneLOop: For the evaluation of one-loop scalar functions*, Comput. Phys. Commun. **182** (2011) 2427 [[arXiv:1007.4716](#) [[hep-ph](#)]].
- [38] G. Ossola, C. G. Papadopoulos and R. Pittau, *Reducing full one-loop amplitudes to scalar integrals at the integrand level*, Nucl. Phys. B **763** (2007) 147 [[hep-ph/0609007](#)].
- [39] S. Catani and M. H. Seymour, *A General algorithm for calculating jet cross-sections in NLO QCD*, Nucl. Phys. B **485** (1997) 291 Erratum: [Nucl. Phys. B **510** (1998) 503] [[hep-ph/9605323](#)].
- [40] S. Catani, S. Dittmaier, M. H. Seymour and Z. Trocsanyi, *The Dipole formalism for next-to-leading order QCD calculations with massive partons*, Nucl. Phys. B **627** (2002) 189 [[hep-ph/0201036](#)].
- [41] G. Bevilacqua, M. Czakon, M. Kubocz and M. Worek, *Complete Nagy-Soper subtraction for next-to-leading order calculations in QCD*, JHEP **1310** (2013) 204 [[arXiv:1308.5605](#) [[hep-ph](#)]].
- [42] G. Bevilacqua, M. Czakon, M. V. Garzelli, A. van Hameren, A. Kardos, C. G. Papadopoulos, R. Pittau and M. Worek, *HELAC-NLO*, Comput. Phys. Commun. **184** (2013) 986 [[arXiv:1110.1499](#) [[hep-ph](#)]].
- [43] G. Bevilacqua, H. B. Hartanto, M. Kraus and M. Worek, *Top Quark Pair Production in Association with a Jet with Next-to-Leading-Order QCD Off-Shell Effects at the Large Hadron Collider*, Phys. Rev. Lett. **116** (2016) no.5, 052003 [[arXiv:1509.09242](#) [[hep-ph](#)]].
- [44] G. Bevilacqua, H. B. Hartanto, M. Kraus and M. Worek, *Off-shell Top Quarks with One Jet at the LHC: A comprehensive analysis at NLO QCD*, JHEP **1611** (2016) 098 [[arXiv:1609.01659](#) [[hep-ph](#)]].
- [45] G. Bevilacqua, H. B. Hartanto, M. Kraus, T. Weber and M. Worek, *Hard Photons in Hadroproduction of Top Quarks with Realistic Final States*, JHEP **1810** (2018) 158 [[arXiv:1803.09916](#) [[hep-ph](#)]].
- [46] J. Alwall *et al.*, *A Standard format for Les Houches event files*, Comput. Phys. Commun. **176** (2007) 300 [[hep-ph/0609017](#)].
- [47] I. Antcheva *et al.*, *ROOT: A C++ framework for petabyte data storage, statistical analysis and visualisation*, Comput. Phys. Commun. **180** (2009) 2499 [[arXiv:1508.07749](#) [[physics.data-an](#)]].
- [48] Z. Bern, L. J. Dixon, F. Febres Cordero, S. Höche, H. Ita, D. A. Kosower and D. Maitre, *Ntuples for NLO Events at Hadron Colliders*, Comput. Phys. Commun. **185** (2014) 1443 [[arXiv:1310.7439](#) [[hep-ph](#)]].
- [49] M. Jezabek and J. H. Kühn, *QCD Corrections to Semileptonic Decays of Heavy Quarks*, Nucl. Phys. B **314** (1989) 1.
- [50] K. G. Chetyrkin, R. Harlander, T. Seidensticker and M. Steinhauser, *Second order QCD corrections to  $\Gamma(t \rightarrow Wb)$* , Phys. Rev. D **60** (1999) 114015 [[hep-ph/9906273](#)].
- [51] M. Cacciari, G. P. Salam and G. Soyez, *The anti- $k_t$  jet clustering algorithm*, JHEP **0804** (2008) 063 [[arXiv:0802.1189](#) [[hep-ph](#)]].
- [52] A. Buckley, J. Ferrando, S. Lloyd, K. Nordström, B. Page, M. Rüfenacht, M. Schönherr and G. Watt, *LHAPDF6: parton density access in the LHC precision era*, Eur. Phys. J. C **75** (2015) 132 [[arXiv:1412.7420](#) [[hep-ph](#)]].

- [53] J. Butterworth *et al.*, *PDF4LHC recommendations for LHC Run II*, J. Phys. G **43** (2016) 023001 [[arXiv:1510.03865](#) [[hep-ph](#)]].
- [54] S. Dulat *et al.*, *New parton distribution functions from a global analysis of quantum chromodynamics*, Phys. Rev. D **93** (2016) no.3, 033006 [[arXiv:1506.07443](#) [[hep-ph](#)]].
- [55] R. D. Ball *et al.* [NNPDF Collaboration], *Parton distributions for the LHC Run II*, JHEP **1504** (2015) 040 [[arXiv:1410.8849](#) [[hep-ph](#)]].
- [56] L. A. Harland-Lang, A. D. Martin, P. Motylinski and R. S. Thorne, *Parton distributions in the LHC era: MMHT 2014 PDFs*, Eur. Phys. J. C **75** (2015) no.5, 204 [[arXiv:1412.3989](#) [[hep-ph](#)]].
- [57] R. Boughezal and M. Schulze, *Precise predictions for top quark plus missing energy signatures at the LHC*, Phys. Rev. Lett. **110** (2013) no.19, 192002 [[arXiv:1212.0898](#) [[hep-ph](#)]].
- [58] R. Boughezal and M. Schulze,  *$t\bar{t}$ +large missing energy from top-quark partners: a comprehensive study at NLO QCD*, Phys. Rev. D **88** (2013) no.11, 114002 [[arXiv:1309.2316](#) [[hep-ph](#)]].
- [59] M. Bauer, U. Haisch and F. Kahlhoefer, *Simplified dark matter models with two Higgs doublets: I. Pseudoscalar mediators*, JHEP **1705** (2017) 138 [[arXiv:1701.07427](#) [[hep-ph](#)]].
- [60] G. Bevilacqua, H. B. Hartanto, M. Kraus, T. Weber and M. Worek, *Precise predictions for  $t\bar{t}\gamma/t\bar{t}$  cross section ratios at the LHC*, JHEP **1901** (2019) 188 [[arXiv:1809.08562](#) [[hep-ph](#)]].